The 5th YRA MedTech Symposium is jointly organized by the FH Aachen, the University of Duisburg-Essen, the Hochschule Hamm Lippstadt and the Westfälische Hochschule

2026

Symposium Proceedings

Editors:

Ilya Digel (FH Aachen)
Daniel Erni (Universität Duisburg-Essen)
Peter Kayser (FH Aachen)
Carole Leguy (HS Ruhr West)
Manfred Staat (FH Aachen)
Christopher Stegmann (HS Hamm-Lippstadt)
Atakan Tepecik (FH Aachen)
Jürgen Trzewik (HS Hamm-Lippstadt)
Waldemar Zylka (Westfälische HS)

Young Researchers Academy – MedTech in NRW

Ph.D., Master, and Bachelor students of all universities in NRW (Uni & FH) working in fields related to (bio)medical engineering present their research or their thesis at the

5th YRA MedTech Symposium 2026

September 17 & 18 2026
FH Aachen UAS/ Juelich Campus
Heinrich-Mussmann-Str. 1
52428 Juelich, Germany
www.yra.fh-aachen.de

ISBN 978-3-940402-91-2
DOI: 10.17185/duepublico/87574

Dear Participants, Colleagues, and Esteemed Guests

It is our great pleasure to warmly welcome you to the YRA MedTech Symposium 2026, taking place on 17–18 September 2026 at Campus Jülich. These proceedings provide a record of the ideas, discussions, and emerging collaborations that shape this year's meeting.

Following the successful re-establishment of the YRA MedTech Symposium in 2024, this year's meeting continues a tradition that began in 2016 by bringing together participants from FH Aachen and other universities, research institutes, clinical environments, and industry. The symposium thereby strengthens both the regional research community and the wider national and international networks from which future collaborations may emerge.

Biomedical engineering brings together physics, biology, medicine, chemistry, materials science, data analysis, electronics, mechanical engineering, and clinical practice. Its most meaningful advances often arise precisely where established disciplinary boundaries become permeable: when a physical principle is translated into a diagnostic method, when a new material is designed around a biological requirement, when sensor data are transformed into clinically relevant information, or when an engineering prototype is evaluated in the context of real human needs.

The Young Researcher Academy was created to provide an open and supportive forum for researchers at the beginning of their scientific careers to engage with this interdisciplinary landscape. The symposium offers bachelor's and master's students, doctoral candidates, and other early-career researchers an opportunity to present work in progress, discuss methods and results, receive constructive feedback, and learn from one another. It is deliberately more than a sequence of scientific presentations. It provides a space in which early-stage ideas can be explored, unexpected connections can be discovered, and young researchers can gain confidence in explaining not only what they have done, but also why their work matters.

The contributions assembled for YRA 2026 vividly demonstrate the breadth and vitality of contemporary medical technology. Several exciting projects explore magnetic nanoparticles, their physical behavior, sustainable synthesis, enzyme immobilization, and their potential roles in imaging, sensing, heating, and theranostic applications. Others address advanced biomaterials, including silk-fibroin vascular grafts, tubular structures, electrospun membranes, and hydrogel-based tissue phantoms designed to reproduce relevant mechanical or electrical properties. These studies illustrate how the development of medical materials requires an unusually close dialogue between fabrication, characterization, modelling, and biological function. A further group of contributions focuses on measurement and diagnostic technologies. The program includes work on retinal imaging and oculomics, the objective detection of spontaneous retinal venous pulsation, magnetic particle spectroscopy, potentiometric sensing, and the reconstruction of anatomical geometries for surgical planning. Together, these projects reflect a central ambition of biomedical engineering: to obtain reliable and clinically meaningful information through methods that are increasingly precise, quantitative, and, wherever possible, minimally invasive.

The 2026 symposium also reaches beyond conventional clinical settings. Research on fluorescence spectroscopy for biosignature detection in icy ocean worlds connects biomedical instrumentation with astrobiology and planetary exploration. Work on current and future spaceflight countermeasures highlights the physiological and technological challenges associated with human spaceflight. Projects involving haptic teleoperation for ultrasound diagnostics, biomimetic motion profiles for the care of preterm infants, radiopharmaceutical transfer systems, and structured learning approaches in higher education further broaden the scientific spectrum.

An important strength of the YRA format is that it brings together different stages of scientific development. Some contributions present mature experimental results, while others introduce simulations, preliminary studies, prototypes, process optimizations, or methodological concepts. All of these stages are essential. Science advances not only through completed projects, but also through carefully formulated questions, transparent limitations, negative or unexpected findings, and the willingness to revise an approach. We therefore encourage all participants to regard discussion and critique not as a final judgement on their work, but as an integral and productive part of the research process.

The YRA2026 keynote program complements this perspective by connecting academic research with broader professional and societal contexts. Insights into the founding of a biotechnology company illuminate the challenges involved in translating a scientific idea into sustainable innovation. Contributions on light-addressable potentiometric sensors demonstrate how fundamental sensing principles can be developed into versatile analytical technologies. Perspectives on spaceflight countermeasures show how interdisciplinary research must respond to demanding operational environments and long-term considerations of human health. Together, these themes remind us that successful medical technology depends not only on scientific novelty, but also on validation, usability, communication, regulation, entrepreneurship, and responsible implementation.

We extend our sincere thanks to all authors, presenters, keynote speakers, reviewers, moderators, supervisors, institutional partners, and members of the organizing team. Their time, expertise, and commitment have made this symposium and the present volume possible. In particular, we thank the young researchers who have chosen this symposium as a platform to present their ideas and who are prepared to discuss their work openly. Their creativity, dedication, and scientific courage give the YRA MedTech Symposium its purpose.

May these two days be characterized by thoughtful questions, constructive exchange, new connections, and the shared enthusiasm that drives biomedical engineering forward. We hope that every participant will leave the symposium with clearer ideas, broader perspectives, and renewed motivation for the next stage of their research.

With best regards,

The Organizing Committee, YRA MedTech Symposium 2026

Ilya Digel
Daniel Erni
Peter Kayser
Carole Leguy
Manfred Staat
Christopher Stegmann
Atakan Tepecik
Jürgen Trzewik
Waldemar Zylka

Agenda YRA MedTech Symposium 2026

DAY 1 | Thursday, September 17, 2026

ARRIVAL AND REGISTRATION (Gerling Pavillon, Heinrich-Mussmann-Str. 1 52428 Juelich)	
NETWORKING	
GREETINGS OPENING AND ORGANIZATIONAL NOTES	
KEYNOTE LECTURE – "Light-addressable potentiometric sensors" **Prof. Dr. Torsten Wagner, Dean, FB 9 Medizintechnik und Technomathematik, FH Aachen** **Institut für Nano- und Biotechnologien (INB)**	
COFFEE BREAK	
Session I: Magnetic Nanoparticle Modeling & Theranostics **Chair: Jürgen Trzewik / Ilya Digel**	**9**
Towards detecting interacting magnetic nanoparticles via MPS in in-vivo conditions: First answers from simulative insight. ***M. B. Abbas*** *and U. M. Engelmann* *Department of Medical Engineering and Applied Mathematics, FH Aachen University of Applied Sciences, 52428 Jülich, Germany*	**10**
One-for-all in theranostics? Simulation-based search for optimally sized nanoparticles for imaging, sensing and heating ***Beril Simsek(1)****, Hans-Joachim Krause(1,2) and Ulrich M. Engelmann(1)* *(1) Department of Medical Engineering and Applied Mathematics, FH Aachen University of Applied Sciences, | D-52428 Jülich, Germany | (2) Institute of Biological Information Processing, Bioelectronics (IBI-3), Forschungszentrum Jülich, D-52428 Jülich, Germany*	**12**
Session discussion	
LUNCH BREAK	
Session II: Diagnostics, Imaging & Physiological Signals **Chair: Atakan Tepecik**	**14**
Reading Disease in the Retina: Oculomics and the Future of Non-Invasive Biomarkers ***Momin Alnemer(1)****, Konstantin Kotliar(1)* *(1) Institute of Bioengineering, Department of Medical Engineering and Technomathematics, Aachen University of Applied Sciences, Jülich Campus*	**15**
Toward Reproducible Abdominal Aortic Diameter Measurement: An In Vivo Pilot Study Comparing Autonomous and Manual Ultrasound Guidance under respiratory movement ***Miedia Ali(1)****, Timo Waschk(1), Richard Lopata (2), Carole Leguy(1)* *Institute MST, University of Applied Sciences Ruhr West, D-45479 Mülheim a.d Ruhr, Germany | Department of Biomedical Engineering, Eindhoven University of Technology, 5612 AZ Eindhoven, The Netherlands*	**17**
Session discussion	
COFFEE BREAK	
Session III: Magnetic Nanoparticles: Synthesis & Functionalization **Chair: Momin Alnemer**	**20**
Synthesis and Characterisation of Superparamagnetic Iron Oxide Nanoparticle/β-Galactosidase bionanohybrid system for biomedical applications ***Semi Hamzacebioglu****, Harini Kopalle, and Maryam Weil* *Faculty of Medical Engineering and Technomathematics, FH Aachen University of Applied Sciences, Campus Jülich, D-52428 Jülich, Germany*	**21**
Session discussion	
POSTER SETUP AND NETWORKING	
POSTER SESSION AND NETWORKING	**40**
DAY 1 SUMMARY + UPDATES	
Social event (BBQ)	
END DAY 1	

POSTER SESSION PARTICIPANTS

Thursday, September 17, 2026

Stand 1	**Sustainable Green Synthesis of Magnetic Iron Oxide Nanoparticles** *David Ayoub, Maryam Weil* *Faculty of Medical Engineering and Technomathematics* *FH Aachen University of Applied Sciences, Campus Jülich, D-52428 Jülich, Germany*	**41**
Stand 2	**Magnetic Iron Oxide Nanoparticle-Based Enzyme Immobilization: A Comparative Kinetic Study** *Edikan Okoko, Maryam Weil* *Faculty of Medical Engineering and Technomathematics* *FH Aachen University of Applied Sciences, Campus Jülich, D-52428 Jülich, Germany*	**43**
Stand 3	**Towards a Sustainable Synthesis of Magnetic Iron Oxide Nanoparticles Through Process Optimization** *Lisa Kissenkötter, David Ayoub and Maryam Weil* *Faculty of Medical Engineering and Technomathematics,* *FH Aachen University of Applied Sciences, Campus Jülich, D-52428 Jülich, Germany*	**45**
Stand 4	**How materials properties govern signal generation in magnetic particle spectroscopy: First answers from simulative insights** *S. Bolte, O. Lawal, and U. M. Engelmann* *Department of Medical Engineering and Applied Mathematics* *FH Aachen University of Applied Sciences, D-52428 Jülich, Germany*	**47**
Stand 5	**Maternal Gait as a Reference Model for Vestibular Stimulation of Preterm Infants: IMU-Based Derivation of a Biomimetic Motion Profile for an Actively Swinging Hammock** *Sude Yildirir(1), Christine Bremer(1), and Andreas Hennig(1)* *(1) Hochschule Ruhr West* *Universty of Appied Sicences* *Institute of Measuring and Sensor Technology, D-45476 Mülheim an der Ruhr*	**49**
Stand 6	**Fluorescence spectroscopy for Biosignature Detection in Icy Ocean Worlds: Insights from the TRIPLE AstroBioLab** *Jacqueline Blok, Ilya Digel* *Institute for Bioengineering,* *FB 9, FH Aachen University of Applied Sciences, 52428, Jülich, Germany*	**51**
Stand 7	**Operating Procedure Adaptation for DNA Sequencing of Sea Water Microbiome for Antarctic Metagenome Analysis** *Isabelle Kamp, Ilya Digel* *Institute for Bioengineering,* *Faculty of Medical Engineering and Technomathematics, University of Applied Sciences Aachen,* *D-52428 Jülich, Germany*	**53**
Stand 8	**Interdigitated Electrodes for Biomedical Applications: Theoretical and Experimental Investigation of Geometric Factors** *Adrian Klautsch(1), Maryam Weil(1), and Xuan-Thang Vu(2)* *(1) Faculty of Medical Engineering and Technomathematics* *FH Aachen University of Applied Sciences, Campus Jülich, D-52428 Jülich, Germany* *(2) Institute of Materials in Electrical Engineering 1,* *Faculty of Electrical Engineering and Information Technology,* *RWTH Aachen University, D-52074 Aachen, Germany*	**54**
Stand 9	**Developing Structured Knowledge in Higher Education Using Kaizen-Based Learning** *Yrza Myktybekova (1), Kalampir Zhumagulova (1), and Ilya Digel (2)* *(1) Department of Biology, Abai Kazakh National Pedagogical University, Almaty, Republic of Kazakhstan,* *(2) Institute for Bioengineering, FH Aachen University of Applied Sciences | Jülich, Germany*	**56**

Agenda YRA MedTech Symposium 2026

DAY 2 | Friday, September 18, 2026

KEYNOTE LECTURE "Biotech from Scratch: Lessons learned from founding a company in the pharmaceutical industry" Dr. Matthias Gossmann, M.Sc. Peter Linder (innoVitro GmbH)	
KEYNOTE LECTURE "Current Spaceflight Countermeasures & Future Developments" Dr. Timo Frett, Research Associate Short Arm Human Centrifuges at German Aerospace Center (DLR)	
COFFEE BREAK	
Session IV: Biomaterials & Tissue Engineering **Chair: Robin Schlinkmann**	**23**
Diameter-Dependent Fabrication and Mechanical Assessment of Layer-by-Layer Silk Fibroin Vascular Grafts Prototypes ***Chorouk Dya(1***,2), Maike Bittner(2,3), Benedetta Isella(2), and Ilya Digel (1)* *(1) Institute for Bioengineering, | FH Aachen University of Applied Sciences, Heinrich-Mussmann-Str. 1, 52428 Jülich, Germany | (2) Fibrothelium GmbH, | Research and Development, Philipstr. 8, Aachen, Germany | (3) School of Engineering and Institute for Health Discovery and Innovation, | University of Galway, | University Road, Galway, Ireland*	**24**
Dip-Coating of Silk Fibroin Tubular Structures for Microvascular Applications: A Parametric Study ***Peace Oduyebo(1) (2)***, *Mariana Rodrigues(2) (3), Benedetta Isella(2) and Ilya Digel(1)* *(1) Institute for Bioengineering, | University of Applied Sciences Aachen, Heinrich-Mußmann-Str. 1, Aachen, Germany | (2) Fibrothelium GmbH, | Research and Development, Phillipstr. 8, Aachen, Germany | (3) Department for Biohybrid & Medical Textiles (BioTex), | AME - Helmholtz Institute for Biomedical Engineering, | RWTH Aachen University, Germany*	**26**
PARAMETER AND MORPHOLOGY ANALYSIS OF ELECTROSPUN SILK FIBROIN MEMBRANES FOR GUIDED BONE REGENERATION ***Robin Schlinkmann***, *Thomas Gries* *ITA – Institut für Textiltechnik RWTH Aachen University 52074 Aachen, Germany*	**28**
Session discussion	
LUNCH BREAK (TECHNICAL TRANSITION, IF NEEDED)	
Session V: Phantoms, Materials & Preclinical Testing **Chair: Timo Waschk**	**30**
Hydrogel Tissue Phantoms for Mimicking Electrical Properties in Laboratory Setups for Preclinical Evaluation ***Johannes Brüning***, *Monika Kolodziej, Thomas Hilbel, and Michael Schlüter* *Westphalian University of Applied Science | Department for Electrical Engineering and Applied Sciences | 45897, Gelsenkirchen, Germany*	**31**
Preliminary Study on the Suitability of PDMS as a Material for Target Transfer Lines ***Tim C. Wichmann(1)***, *Johannes Brüning(2), Michael Schlüter(2) and Michael Nader(1)* *(1) Department of Nuclear Medicine, Division of Radiopharmacy | Faculty of Medicine, University Duisburg-Essen | D-45147 Essen, Germany | (2) Lab for Microsystems Technology | Faculty of Physical Engineering, Westphalian University of Applied Sciences | D-45897 Gelsenkirchen, Germany*	**33**
Session discussion	
Session VI: Medical Devices, Robotics & Biomechanics **Chair: Christopher Stegmann**	**35**
Design and implementation of a communication interface for cobot teleoperation with haptic feedback in ultrasound diagnostics ***Timo Waschk(1)***, *Soufian Benchaou(1), Carole Leguy(1) and Richard Lopata(2)* *(1) Institute of measurement and sensor technology, University of Applied Sciences Ruhr West, | D-45479 Mülheim, Germany | (2) Photoacoustics & Ultrasound Laboratory, | Department of Biomedical Engineering, Eindhoven University of Technology, NL-5612 AE Eindhoven, Netherlands*	**36**
Preoperative Reconstruction of Femoral Stem Geometry for Combined Target Zone Planning in Total Hip Arthroplasty ***Mohammed Aouad*** [1], *Luisa Berger* [2], *Klaus Radermacher* [2], *and Ilya Digel* [1] *(1) Faculty of Medical Engineering and Technomathematics (FB09), | FH Aachen - University of Applied Sciences, Campus Jülich, | D-52428 Jülich, Germany | (2) mediTEC - Chair of Medical Engineering, | Helmholtz-Institute for Biomedical Engineering, RWTH Aachen University, D-52074 Aachen, Germany*	**38**
Session discussion	
SUMMARY, CONCLUDING DISCUSSION AND ANNOUNCEMENTS	
COFFEE & FAREWELL	
END	

Session I: Magnetic Nanoparticle Modeling & Theranostics

Towards detecting interacting magnetic nanoparticles via MPS in *in-vivo* conditions: First answers from simulative insight.

M. B. Abbas(1) and U. M. Engelmann(1)

(1) Department of Medical Engineering and Applied Mathematics,
FH Aachen University of Applied Sciences,
52428 Jülich, Germany
E-Mail: mohamad.abbas@alumni.fh-aachen.de | engelmann@fh-aachen.de

Abstract – Magnetic nanoparticles (MNP) are key in biomedical imaging and therapy, but their magnetic response is affected by physiological conditions in vivo. This study uses coupled Néel–Brownian relaxation simulations to assess how immobilization, confinement, and increased viscosity, which all commonly occur during in vivo application of MNP, alter magnetic particle spectroscopy (MPS) signals. The preliminary results reveal a remarkable reduction in signal intensity for gradually immobilized and strongly interacting MNP and highlighting detection challenges for interacting particles in physiological environments expected during in vivo biomedical applications.

Introduction: For *in-vivo* applications such as magnetic particle imaging (MPI) or magnetic particle Hyperthermia (MPH), magnetic nanoparticles (MNP) will be administered into the bloodstream. Within hours of circulation time [1], the particles typically accumulate at target sites e.g. tumors, bind to target biomolecules or become internalized by cells [2]. This inevitably leads to a reduction in interparticle distance, d, and restricted mobility, i.e. a more viscous surrounding environment. A higher viscosity, η, will slow the Brownian relaxation time, $\tau_B \propto \eta$, resulting in a slower MNP response to the applied field, $H(t)$ [3]. On the other hand, reducing d results in stronger magnetic coupling between neighboring MNP, due to magnetic dipole particle-particle interactions (pp-IA), whose energy, ε_{pp-IA}, becomes comparable to the energy of the applied field as well as thermal energy [4]. ε_{pp-IA} exerted on an individual particle with magnetic moment, $|\boldsymbol{m}_0| = M_S V_{C,0} = M_S \cdot \frac{4}{3}\pi d_{C,0}^3$, located at an arbitrary point d_0, where all other particles ($\boldsymbol{m}_i$) are a distance d_i away from d_0, reads:

$$\varepsilon_{pp-IA} = \sum_i \frac{\mu_0}{4\pi d_i^3}\left(\frac{3(\boldsymbol{m}_0 \cdot d_0)\cdot(\boldsymbol{m}_i \cdot d_i)}{d_i^2} - \boldsymbol{m}_0 \cdot \boldsymbol{m}_i\right) \quad (1)$$

This work is dedicated to study the influence of pp-IA and viscosity on the 3rd harmonic signal of magnetic particle spectroscopy (MPS) by gradually decreasing interparticle distance between MNP and increasing viscosity of the surrounding environment.

Methodology: Using stochastic Neel-Brownian coupled dynamic relaxation simulations [5], we predict the magnetic response of magnetite MNP ($\rho_{Fe_3O_4} = 5{,}2\ \mathrm{g\,cm^{-3}}$, $M_S = 476\ \mathrm{kA\,m^{-1}}$, $K = 11\ \mathrm{kJ\,m^{-3}}$ (uniaxial), $T = 310\ \mathrm{K}$) to a field of $H(t) = H \cdot \sin(2\pi f t)$ with $H = 25\ mT{\mu_0}^{-1}$ and $f = 25\ \mathrm{kHz}$. We simulated three core sizes $d_C = (15, 20, 25)\ \mathrm{nm}$ with monodisperse log-normal size distribution width $\sigma = 0.05$ each with hydrodynamic size $d_H = 50\ \mathrm{nm}$. We probed average interparticle distances, $d_{Avg} = (d_H, 2d_H, 3d_H)$ (i.e. particle shells touch for $d_{Avg} = d_H$), and effective viscosities, $\eta = (0.80, 50, 500, 5000)$ mPa·s, representing physiological values for MNP *in-vivo* [6].

Results and discussion: Comparing MPS signals for $d_{Avg} = 3d_H = 150\ \mathrm{nm}$ (non-interacting particles) to $d_{Avg} = d_H = 50\ \mathrm{nm}$, Fig. 1A shows a size-dependent signal reduction by: ~85% ($d_C = 25\ \mathrm{nm}$), ~43% ($d_C = 20\ \mathrm{nm}$) and ~0% ($d_C = 15\ \mathrm{nm}$) with ppIA. Additionally, increasing viscosities cause a general signal reduction by (6 – 12)% independent of d_C and r_{Avg}. Fig. 1B depicts d_{Avg} and d_C dependency for water viscosity, showing generally strongest signal for largest particles, i.e. largest magnetic moments, when ppIA is negligible for $d_{Avg} = 150\ \mathrm{nm}$, while onset of ppIA increasingly and remarkably diminishes the signal (as discussed above), rendering $d_C = 20\ \mathrm{nm}$ most effective in absolute values, while the ppIA is negligible for $d_C = 15\ \mathrm{nm}$ MNP.
Remarkably, the interpretation changes for dose-dependent considerations, shown in Fig. 1C, where the same MPS signal data was normalized to the absolute amount of magnetic material present,

calculated from $m_{Fe_3O_4} = \rho_{Fe_3O_4} \cdot n_p \cdot exp\left(\frac{9}{2} \cdot \sigma^2\right) \cdot \frac{\pi}{6} \cdot {d_C}^3$. Under these conditions, the strong ppIA effect on large MNP with $d_C = 25\,\mathrm{nm}$ is outperformed by the mid-size particles of $d_C = 20\,\mathrm{nm}$ for $d_{Avg} \geq 100$ nm, while the MPS signal size-dependence is reversed for strong ppIA ($d_{Avg} = 50\,\mathrm{nm}$), rendering the MPS signal for $d_C = 15$ nm far stronger than that of larger particles. This illustrates the importance of finding a balance between large magnetic moments and suppressed magnetic relaxation at larger core sizes under in-vivo conditions. To further elaborate this phenomenon, Fig. 1D shows the MPS signal (Fig. 1B) in dependence of the ratio of $\varepsilon_{pp-IA} \propto |\boldsymbol{m}|^2/{d_{Avg}}^3 \propto d_C^6/d_{Avg}^3$ derived from Eq. (1) where $|\boldsymbol{m}| \propto {d_C}^3$, as a "ppIA-parameter" for gauging the interaction-strength in a given MNP-physiological-situation. From this, one can derive the preliminary conclusion that for strong ppIA ($d_C^6/d_{Avg}^3 < 0.2\,\mathrm{a.u.}$), approx. 20nm MNP dominate the MPS signal, while low/no ppIA ($d_C^6 \geq 0.2\,\mathrm{a.u.}$), larger particles generally deliver overall better MPS signals. Additionally, viscosity effects matter, but mainly as a modulating factor of secondary importance.

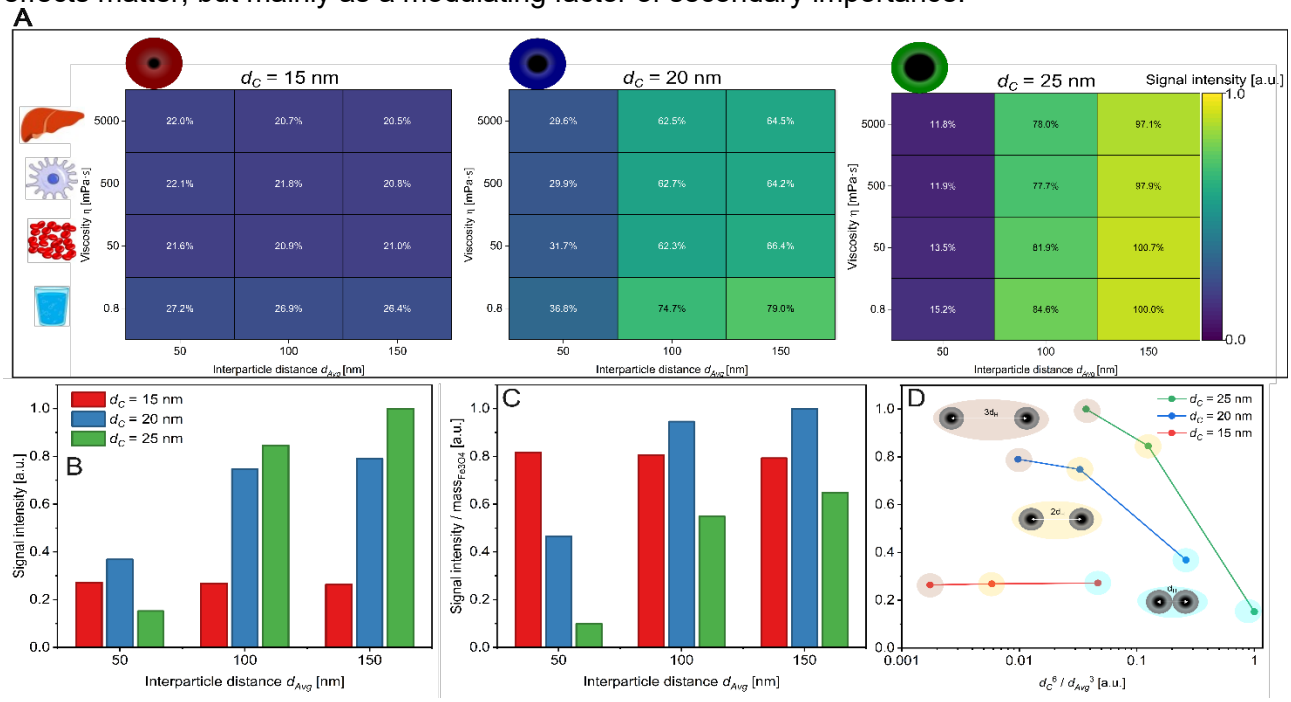

Fig.1: (A) MPS signal intensity as a function of average interparticle distance $d_{Avg} = d_H, 2d_H, 3d_H = (50, 100, 150)$ nm and viscosity η = water, blood, cells, tissue = (0.8, 50, 500, 5000) $\mathrm{mPa \cdot s}$ for the core sizes $d_C = (15, 20, 25)$ nm. (B) Results for water viscosity (B) dependent on interparticle distance and (C) normalized to magnetic mass, i.e. dose-dependent conditions. (D) MPS signal intensity as a function of the "ppIA-parameter" $\varepsilon_{pp-IA} \propto |\boldsymbol{m}|^2/{d_{Avg}}^3 \propto d_C^6/d_{Avg}^3$ (see text).

References

[1] H. Arami, A. Khandhar, D. Liggitt, and K. M. Krishnan, "In vivo delivery, pharmacokinetics, biodistribution and toxicity of iron oxide nanoparticles", *Chemical Society reviews*, vol. 44, no. 23, pp. 8576–8607, 2015, doi: 10.1039/c5cs00541h.

[2] I. Slabu, et al., "Modeling of magnetoliposome uptake in human pancreatic tumor cells in vitro", *Nanotechnology*, vol. 30, no.18, p. 184004, 2019, doi: 10.1088/1361-6528/ab033e

[3] M. B. Abbas, A. M. Pourshahidi, H.-J. Krause, and U. M. Engelmann, "How MNP respond to dual-frequency magnetic excitation in viscous media", *International Journal on Magnetic Particle Imaging*, vol. 11, no. 1, 2025, doi: 10.18416/IJMPI.2025.2503033.

[4] M. B. Abbas, Merle Kott, H-, J. Krause and U. M. Engelmann, "Strong magnetic interaction potentially favors smaller particles in MPS", *International Journal on Magnetic Particle Imaging*, vol. 12, no. 1, 2026, doi: 10.18416/IJMPI.2026.2603015.

[5] U. M. Engelmann, C. Shasha and I. Slabu, "Magnetic Nanoparticle Relaxation in Biomedical Application" in *Magnetic Nanoparticles in Human Health and Medicine*, 1st ed., C. Caizer, Ed. Hoboken, John Wiley & Sons, 2021, pp. 327–354, doi: 10.1002/9781119754725.ch15.

[6] S. Bolte, B. Simsek, M. B. Abbas and U. M . Engelmann, "Large core & small shell particles facilitate physiological viscosity differentiation via MPS", *International Journal on Magnetic Particle Imaging*, vol. 12, no. 1, 2026, doi: 10.18416/IJMPI.2026.2603047

One-for-all in theranostics? Simulation-based search for optimally sized nanoparticles for imaging, sensing and heating

Beril Simsek[1], Hans-Joachim Krause[1,2] and Ulrich M. Engelmann[1]

[1] Department of Medical Engineering and Applied Mathematics,
FH Aachen University of Applied Sciences,
D-52428 Jülich, Germany
[2] Institute of Biological Information Processing,
Bioelectronics (IBI-3), Forschungszentrum Jülich,
D-52428 Jülich, Germany
E-mail: beril.simsek@alumni.fh-aachen.de | engelmann@fh-aachen.de

Abstract – Magnetic nanoparticles (MNPs) enable biomedical applications in magnetic particle spectroscopy (MPS) and imaging (MPI), frequency-mixing magnetic detection (FMMD), and magnetic fluid hyperthermia (MFH). All these techniques rely on the magnetic relaxation of MNPs and are influenced by particle core size, while the modality is selected through the applied alternating magnetic field (AMF). This study uses Néel-Brownian relaxation simulations to identify the optimal core size of iron-oxide MNPs that maximizes signal performance across all applications under standard AMF conditions simultaneously. Preliminary results identify monodisperse MNPs with 20 nm core size as ideal candidates, guiding MNP design for direct use in theranostics.

Methods – We performed stochastic Néel–Brown simulations [1] for ensembles of 1000 particles across a broad range of mean core sizes ($d_c = 10 - 30$ nm) and lognormal distribution widths ($\sigma = 0.05 - 0.45$) assuming a hydrodynamic diameter of $d_H = 100$ nm and a water-like viscosity of $\eta = 0.89$ cP. We simulated non-interacting magnetite MNPs with density $\rho_{Fe_3O_4} = 5200\ \mathrm{kg\ m^{-3}}$, saturation magnetization $M_S = 476\ \mathrm{kA\ m^{-1}}$, magnetic anisotropy constant $K = 11\ \mathrm{kJ\ m^{-3}}$ (uniaxial), and temperature $T = 300\ \mathrm{K}$. For each modality, we applied representative sinusoidal field parameters to the MNP ensemble, as summarized in Table 1 [2].

Table 1: AMF parameters used for each modality: MPI and MFH use single-frequency $H(t) = H_{ac} \cdot \sin(2\pi \cdot f \cdot t) + H_0$, whereas FMMD uses dual-frequency excitation $H(t) = H_{LF} \cdot \sin(2\pi \cdot f_{LF} \cdot t) + H_{HF} \cdot \sin(2\pi \cdot f_{HF} \cdot t) + H_0$.

	Imaging (MPI/MPS)	Sensing (FMMD)	Heating (MFH)
Field amplitude [mT/μ$_0$]	$H_{ac} = 20$; $H_0 = 0$	$H_{LF} = 1.2$; $H_{HF} = 16$; $H_0 = (0,1,\dots,24)$	$H_{ac} = 25$ $H_0 = 0$
Frequency [kHz]	$f = 25$	$f_{LF} = 2$; $f_{HF} = 40$	$f = 250$

From the simulated $M(H)$ curves, we extracted three modality-specific performance metrics: the third-harmonic amplitude A_3 for MPI/MPS, the specific loss power (SLP) derived from the hysteresis-loop area for MFH, and the peak intermodulation magnetic moment for FMMD under a varying offset field (Table 1). Further details of the analysis are provided in Refs. [2] and [3]. Each metric was normalized by the total magnetic mass $m_{Fe_3O_4} = \rho_{Fe_3O_4} \cdot n_p \cdot exp\left(\frac{9}{2} \cdot \sigma^2\right) \cdot \frac{\pi}{6} \cdot {d_c}^3$ and subsequently min–max scaled to the interval $[0,1]$, yielding dose-normalized values. The three normalized scores were then combined using an equally weighted geometric mean $S = \left(\widehat{A_3} \cdot \widehat{SLP} \cdot \widehat{m_{(f_1+f_2)}}\right)^{(1/3)}$ to quantify the balanced suitability of each MNP formulation (d_c and σ) across all three modalities.

Results and Discussion – Figure 1 shows the modality-specific performance metrics ($A_3, SLP, m_{f_1+f_2}$) as functions of mean core diameter and distribution width on a star-glyph map: The lengths of the three glyph arms represent the normalized MPI/MPS, MFH, and FMMD signals, respectively. The underlying grayscale map shows the combined geometric-mean score S and identifies ideal particle sizes (d_c and σ) that perform consistently well across all three modalities.

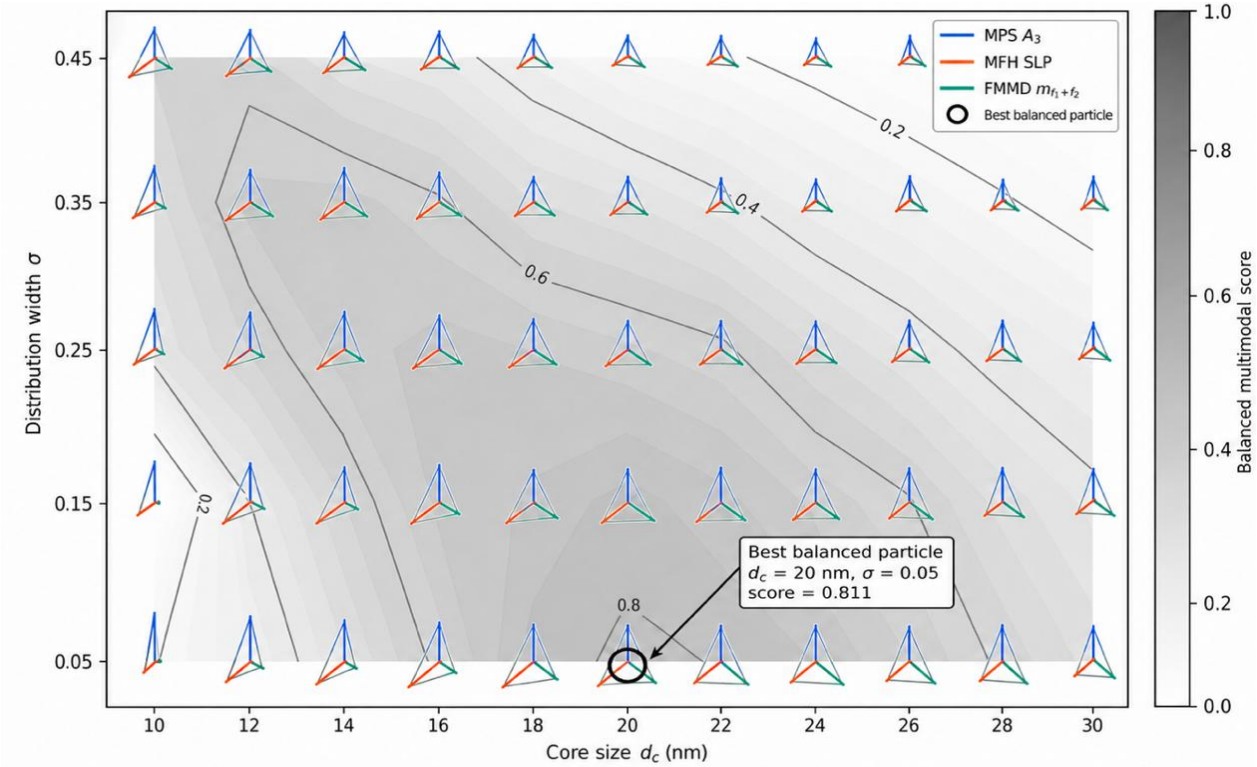

Fig. 1. Star-glyph representation of multimodal MNP performance as a function of core diameter d_c and distribution width σ. The glyph arms represent the normalized performance metrics for MPS (blue), MFH (red), and FMMD (green). The background shows the equally weighted geometric-mean score S. The circled design indicates the best-balanced formulation with the highest combined multimodal score.

The highest balanced multimodal performance was obtained for highly monodisperse, mid-sized MNPs ($d_c = 20\ \mathrm{nm},\ \sigma = 0.05$), with a combined score of $S = 0.811$ (corresponding normalized individual scores: $\widehat{A_3} = 0.631$, $\widehat{SLP} = 0.958$, $\widehat{m_{(f_1+f_2)}} = 0.882$). When highly monodisperse MNPs are unavailable, for example, when using co-precipitation methods [4], increasing polydispersity shifts the optimal mean core diameter towards smaller values, reaching approximately $d_c = 12\ \mathrm{nm}$ at $\sigma = 0.35$. These preliminary results provide guidance for selecting MNP core-size distributions for either modality-specific applications or balanced multimodal theranostic use.

Conclusion – Our preliminary results establish a simulation-based framework for comparing iron-oxide MNP designs across sensing, imaging, and heating applications. Within the investigated parameter space, highly monodisperse MNPs with a mean core diameter of $20\ nm$ provided the best-balanced multimodal performance across MPI/MPS, MFH and FMMD. Future work will extend the study to viscosities representative of blood, intracellular environments, and soft tissue environments in conjunction with examining the effects of magnetic interparticle interactions.

References

[1] U. M. Engelmann, C. Shasha and I. Slabu, “Magnetic Nanoparticle Relaxation in Biomedical Application” in *Magnetic Nanoparticles in Human Health and Medicine*, 1st ed., C. Caizer, Ed. Hoboken, John Wiley & Sons, 2021, pp. 327–354, doi: 10.1002/9781119754725.ch15.

[2] H.-J. Krause and U. M. Engelmann, “Fundamentals and Applications of Dual-Frequency Magnetic Particle Spectroscopy: Review for Biomedicine and Materials Characterization”, *Advanced Science*, vol. 12, no. 13, Art. no. 2416838, 2025, doi: 10.1002/advs.202416838.

[3] B. Simsek, S. R. S. S. V. Ganni, H.-J. Krause and U. M. Engelmann, “In search of multifunctional magnetic nanoparticle design with micromagnetic simulations”, International Journal on Magnetic Particle Imaging, vol. 11, no. 1, 2025, doi: 10.18416/IJMPI.2025.2503049.

[4] U. M. Engelmann, “Assessing Magnetic Fluid Hyperthermia: Magnetic Relaxation Simulation, Modeling of Nanoparticle Uptake inside Pancreatic Tumor Cells and in vitro Efficacy”, Infinite Science Publishing, 2019, ISBN: 978-3945954584.

Session II: Diagnostics, Imaging & Physiological Signals

Reading Disease in the Retina: Oculomics and the Future of Non-Invasive Biomarkers

Momin Alnemer[(1)] and Konstantin Kotliar[(1)]

[(1)] Institute for Bioengineering, Department of Medical Engineering and Technomathematics, Aachen University of Applied Sciences, Jülich Campus
E-Mail: alnemer@fh-aachen.de; kotliar@fh-aachen.de

Abstract – Medicine has long aimed to glimpse inside the living body without opening it, and digitization is quietly changing what that means. Early tools turned hidden physiology into measurable signals, such as electrical activity at the skin, cuff pressure, light absorbed by blood, and anatomy reconstructed from radiation or magnetic fields. Yet a digitized reading was underutilized until later analysis revealed how much information it contained all along. For instance, the electrocardiogram was originally designed to record the heart's electrical signals, and for many years, that was its sole purpose. However, when examined differently, the same familiar trace can now identify issues like a failing pump or mechanical faults it was never intended to detect [1].

That is not an isolated trick. Full spirometry curves outperform standard indices [2], pulse-oximetry waveforms predict fluid responsiveness [3], arterial-pressure waveforms anticipate hypotension [4], and routine histology reveals a tumour's molecular profile [5]. A smartwatch's photoplethysmography sensor follows the same rule. Built only to report a single heart-rate number, it was later analysed instead for temporal irregularity. When investigated across more than 419,000 participants in the Apple Heart Study, it became a clinically meaningful screening tool for atrial fibrillation [6].

The retina may be the richest next case. It is one of the few places where neural tissue and the human microvasculature can be examined directly and repeatedly, without surgery or contrast agents. Retinal structure and vascular health are already linked to cardiovascular, cerebrovascular, kidney, metabolic, and neurodegenerative disease. These links are examples of the evidence base oculomics draws on. Oculomics is a rapidly growing field built on treating the eye as a biomarker for disease elsewhere in the body [7]. Available tools span fundus photography, optical coherence tomography, angiography, and functional vessel recordings, but they have developed unevenly. Their analytical conventions were not designed for the data the field now collects. They were built for a time when computational resources were limited, large labeled datasets did not exist, and validated pipelines for complex time-resolved signals were out of reach.

This gap is largest in dynamic retinal vessel analysis. A typical flicker-light test records several thousand image frames of arterial and venous diameter over roughly six minutes [8]. The reported result is usually just a few numbers, such as baseline diameter, maximum dilation, and sometimes post-flicker constriction. Reaching them means averaging spatial detail into a single trace, merging repeated cycles, and compressing the whole time-course into one peak value (Figure 1). Those numbers are useful, but they are not the full recording. Individual-cycle timing and baseline fluctuation can be preserved [9], the dilation time course characterised [10], and spontaneous, location-dependent oscillation quantified [11]. Early work shows that spatial profiles along the vessel [12], pulse-wave velocity [13], and combined time-and-space analyses [11] are measurable and may capture patterns the peak value misses. This evidence is still preliminary, but it shows retinal vessel dynamics can be read in more than one way.

None of this means simply extracting more variables or pointing artificial intelligence at every recording. Dynamic signals are sensitive to eye motion, tracking errors, protocol design, filtering choices, and endpoint definitions [8,14]. Many candidate features have only been tested in small cohorts with custom methods and little independent replication. Real progress needs richer source data, standardized acquisition, and reproducibility confirmed across visits and devices. It also needs physiological interpretation tied to clinical outcomes. Established measurements should stay the reference point that any new temporal, spatial, or multivariate feature is validated against [8,14].

Timing, shape, location, and rhythm have so far been read separately. The next generation of retinal biomarkers may come from reading them together and letting more systematic analysis validate the combined signal and turn it into an interpretable result. Done well, this could move oculomics beyond

isolated associations. It could become an empirical non-invasive way to detect disease earlier, assess its risk, and track its course over time.

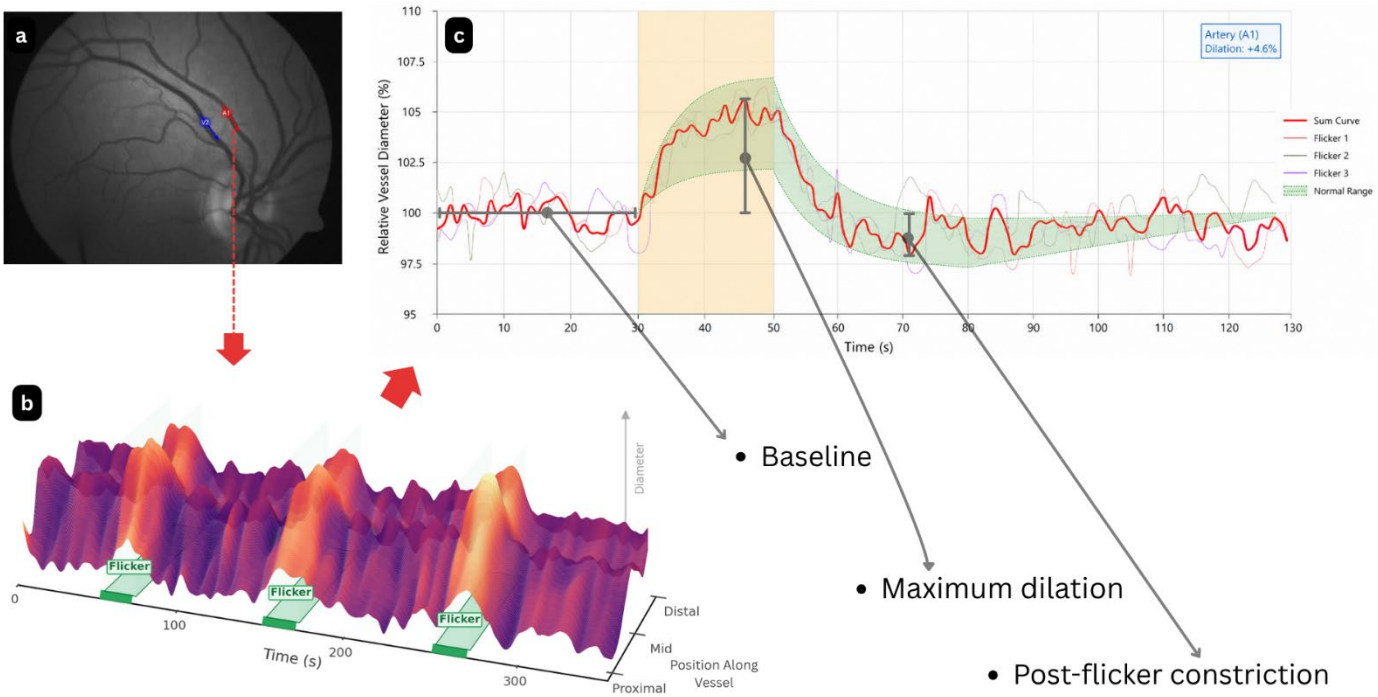

Fig. 1: Overview of the dynamic retinal vessel analysis workflow. (a) Grayscale retinal video with the analysed arterial and venous segments, (b) three-dimensional representation of diameter changes along the arterial vessel segment over the full recording, and (c) spatially averaged flicker response with the conventional parameters baseline, maximum dilation, and post-flicker constriction. The figure shows that the reported parameters are derived from a substantially richer recording, whose additional spatial and temporal features may warrant further investigation. Source: Author's own figure based on data acquired with the Dynamic Vessel Analyzer (DVA®, IMEDOS Systems GmbH, Jena, Germany).

References

[1] Z. I. Attia, S. Kapa, F. Lopez-Jimenez, et al., "Screening for cardiac contractile dysfunction using an artificial intelligence-enabled electrocardiogram," *Nat. Med.*, vol. 25, no. 1, pp. 70-74, 2019, doi: 10.1038/s41591-018-0240-2.
[2] S. Bodduluri, A. Nakhmani, J. M. Reinhardt, et al., "Deep neural network analyses of spirometry for structural phenotyping of chronic obstructive pulmonary disease," *JCI Insight*, vol. 5, no. 13, e132781, 2020, doi: 10.1172/jci.insight.132781.
[3] M. Cannesson, O. Desebbe, P. Rosamel, et al., "Pleth variability index to monitor the respiratory variations in the pulse oximeter plethysmographic waveform amplitude and predict fluid responsiveness in the operating theatre," *Br. J. Anaesth.*, vol. 101, no. 2, pp. 200-206, 2008, doi: 10.1093/bja/aen133.
[4] F. Hatib, Z. Jian, S. Buddi, et al., "Machine-learning algorithm to predict hypotension based on high-fidelity arterial pressure waveform analysis," *Anesthesiology*, vol. 129, no. 4, pp. 663-674, 2018, doi: 10.1097/ALN.0000000000002300.
[5] J. N. Kather, A. T. Pearson, N. Halama, et al., "Deep learning can predict microsatellite instability directly from histology in gastrointestinal cancer," *Nat. Med.*, vol. 25, pp. 1054-1056, 2019, doi: 10.1038/s41591-019-0462-y.
[6] M. V. Perez, K. W. Mahaffey, H. Hedlin, et al., "Large-scale assessment of a smartwatch to identify atrial fibrillation," *N. Engl. J. Med.*, vol. 381, no. 20, pp. 1909-1917, 2019, doi: 10.1056/NEJMoa1901183.
[7] Z. Zhu, Y. Wang, Z. Qi, et al., "Oculomics: Current concepts and evidence," *Prog. Retin. Eye Res.*, vol. 106, 101350, 2025, doi: 10.1016/j.preteyeres.2025.101350.
[8] L. Streese, G. Lona, J. Wagner, et al., "Normative data and standard operating procedures for static and dynamic retinal vessel analysis as biomarker for cardiovascular risk," *Sci. Rep.*, vol. 11, 14136, 2021, doi: 10.1038/s41598-021-93617-7.
[9] R. Heitmar, A. D. Blann, R. P. Cubbidge, G. Y. H. Lip, and D. Gherghel, "Continuous retinal vessel diameter measurements: the future in retinal vessel assessment?" *Invest. Ophthalmol. Vis. Sci.*, vol. 51, no. 11, pp. 5833-5839, 2010, doi: 10.1167/iovs.09-5136.
[10] R. J. Summers and R. Heitmar, "Characterising the time course of the dilatory response of healthy retinal arteries during flicker-light provocation," *J. Vasc. Res.*, vol. 62, pp. 1-9, 2025, doi: 10.1159/000541443.
[11] A. Assaf, K. Kotliar, A. Schmidt-Trucksaess, and I. M. Lanzl, "Multimodal dynamic retinal vessel analysis offers new insights in microvascular defects in Fabry's disease," *Sci. Rep.*, vol. 15, 19867, 2025, doi: 10.1038/s41598-025-03020-9.
[12] K. E. Kotliar, B. Muecke, W. Vilser, R. Schilling, and I. M. Lanzl, "Effect of aging on retinal artery blood column diameter measured along the vessel axis," *Invest. Ophthalmol. Vis. Sci.*, vol. 49, no. 5, pp. 2094-2102, 2008, doi: 10.1167/iovs.07-0711.
[13] K. E. Kotliar, M. Baumann, W. Vilser, and I. M. Lanzl, "Pulse wave velocity in retinal arteries of healthy volunteers," *Br. J. Ophthalmol.*, vol. 95, no. 5, pp. 675-679, 2011, doi: 10.1136/bjo.2010.181263.
[14] H. Hanssen, L. Streese, and W. Vilser, "Retinal vessel diameters and function in cardiovascular risk and disease," *Prog. Retin. Eye Res.*, vol. 91, 101095, 2022, doi: 10.1016/j.preteyeres.2022.101095.

Toward Reproducible Abdominal Aortic Diameter Measurement: An In Vivo Pilot Study Comparing Autonomous and Manual Ultrasound Guidance under respiratory movement

Miedia Ali[(1)], Timo Waschk[(1)], Prof. Dr. Richard Lopata [(2)], Prof. Dr. Carole Leguy[(1)]

(1) Institut MST, University of Applied Sciences Ruhr West, D-45479 Mülheim a.d Ruhr, Germany
(2) Department of Biomedical Engineering, Eindhoven University of Technology, 5612 Az Eindhoven, The Netherlands

Correspondence:
E-Mail: carole.leguy@hs-ruhrwest.de
Web: www.hochschule-ruhr-west.de

Introduction: Ultrasound imaging is a non-invasive modality widely used in vascular assessment. For the abdominal aorta, transabdominal 2D ultrasonography enables measurement of luminal diameter, a key parameter for detecting dilatation and screening for abdominal aortic aneurysm (AAA) [1]. Conventionally, such measurements rely on manual probe guidance, where image quality and diameter accuracy depend on operator-applied contact force, introducing inter-operator variability, inconsistent positioning, and reduced signal-to-noise ratio (SNR) from non-uniform tissue coupling. These factors limit reproducibility and constrain applicability to advanced modalities requiring temporally consistent acquisition, such as 3D vascular reconstruction [2].
Robotic ultrasound systems have been proposed to address these limitations by enabling standardized, reproducible probe trajectories independent of operator skill [2,4,5]. This study employed a collaborative six-degree-of-freedom robotic arm (UR3e) with force-controlled contact and predefined trajectory execution to maintain consistent probe-tissue coupling. While prior work has demonstrated feasibility using phantom models [2,3,4], comparative performance against manual guidance under physiologically realistic conditions, particularly with respiratory motion and probe repositioning, remains inadequately characterized.
This in vivo study evaluates abdominal aortic diameter measurement accuracy via robotic versus manual ultrasound guidance in freely breathing subjects (Fig. 1).

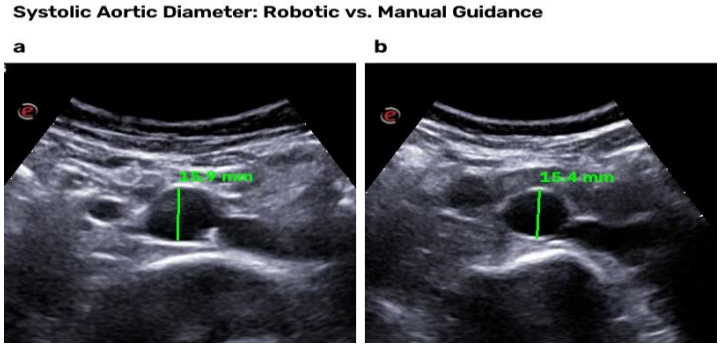

Fig.1: Representative ultrasound frames of the abdominal aorta at matched systolic phase for the same subject, acquired under (a) robotic and (b) manual probe guidance. The green line indicates the manually measured luminal diameter at each respective time point.

Methods: Eight healthy volunteers (3 male, 5 female; age 24–44 years; BMI 21–33 kg/m²) were scanned using a MyLab™9 ultrasound system (Esaote S.p.A., Genoa, Italy) under four conditions, combining robotic and manual probe guidance with breath-hold and free-breathing states. Robotic acquisitions were performed with a collaborative six-degree-of-freedom arm (UR3e, Universal Robots, Odense, Denmark), which followed a predefined trajectory while maintaining a constant contact force of 3–7 N. This study was approved by the local research ethics committee (HRW).

To quantify image quality between guidance modes, signal-to-noise ratio (SNR) was computed per extracted frame as the ratio of the mean pixel intensity within a central signal region-of-interest (μ_{signal}) to the standard deviation of pixel intensity within a background noise region (σ_{noise}). Robotic acquisitions were additionally constrained to cycles falling within a target contact-force range of 3–7 N, a criterion unavailable for manual guidance since no force data were recorded in that condition. Robotic and manual measurements were compared per subject using a one-sample t-test.

Throughout each acquisition, ultrasound video, ECG and robot position, including force data, were recorded synchronously. Aortic diameter was measured via manual caliper-style annotation, using a two-point click on individual frames. For each acquisition, three consecutive cardiac cycles were analyzed. Over the course of each heart cycle, ten candidate frames were selected at regular time intervals, at which a measurement of the aortic diameter was taken. The minimum and maximum diameters from each heart cycle were then used to calculate the mean diastolic and systolic diameters, respectively.

Results: Image quality, quantified via signal-to-noise ratio, was significantly higher under robotic guidance (robotic: 1.16 [IQR 0.95–1.27]; manual: 1.01 [IQR 0.86–1.19]; paired one-sample t-test, p = 0.011). Aortic diameters were comparable between robotic and manual guidance across both cardiac phases (robotic: 14.20 mm [IQR 13.24–15.99] systolic, 11.40 mm [IQR 10.77–14.33] diastolic; manual: 13.20 mm [IQR 11.90–14.98] systolic, 11.50 mm [IQR 10.59–11.94] diastolic; overall diameter 12.59 mm [IQR 12.00–15.47] vs. 12.07 mm [IQR 11.50–13.27]), as shown in Figure 2. None of the diameter differences reached statistical significance (overall diameter: p = 0.054; systole diameter: p = 0.064; diastole diameter: p = 0.076), nor did pulsatility (p = 0.876).

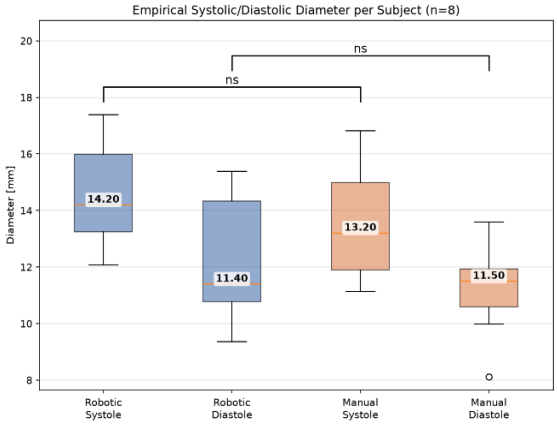

Fig. 2: Empirical systolic and diastolic aortic diameter per subject, robotic vs. manual guidance (n = 8). Significance brackets denote the result of a paired one-sample t-test on the per-subject differences (Robotic − Manual) against zero (ns = not significant, p > 0.05).

Discussion: These preliminary findings suggest that robotic and manual guidance achieved comparable aortic diameter measurements across both cardiac phases. Image quality SNR was found to be higher under robotic guidance, consistent with more stable, force-controlled probe-tissue coupling. However, the observed diameter differences (0.92–1.07 mm) remained within the range of intra-observer measurement noise (SD 1.47 mm), warranting cautious interpretation given the current sample size Frame selection also differed between conditions: robotic acquisitions could additionally be constrained by contact-force and position data, unavailable for manual guidance. This asymmetry may contribute to the observed differences and warrants further investigation. Future work will incorporate automated segmentation, the generalized contrast-to-noise ratio (gCNR) and a larger cohort.

References

[1] Vera H. J. van Hal, Lisanne T. F. Passier, Marc R. H. M. van Sambeek, Hans-Martin Schwab & Richard G. P. Lopata Strain imaging in abdominal aortic aneurysms using bistatic dual-aperture ultrasound. *Sci Rep* **15**, 39892 (2025). https://doi.org/10.1038/s41598-025-23710-8

[2] Ning, G., Chen, J., Zhang, X. *et al.* Force-guided autonomous robotic ultrasound scanning control method for soft uncertain environment. *Int J CARS* **16**, 2189–2199 (2021). https://doi.org/10.1007/s11548-021-02462-6

[3] de Hoop, H., Maas, E., Muller, J.-W., Schwab, H.-M., & Lopata, R. (2025). 3-D motion tracking and vascular strain imaging using bistatic dual aperture ultrasound acquisitions. *Physics in Medicine & Biology*, 70, 045013. https://doi.org/10.1088/1361-6560/ad9db2

[4] Waschk, Timo and Leguy, Carole. "Evaluation of the reconstruction accuracy of 3D robotic ultrasound on in-vitro phantoms for the geometrical characterization of abdominal aortic aneurysms" *Current Directions in Biomedical Engineering*, vol. 11, no. 1, 2025, pp. 517-520. https://doi.org/10.1515/cdbme-2025-0231

[5] Chen, S., Li, Z., Lin, Y. *et al.* Automatic ultrasound scanning robotic system with optical waveguide-based force measurement. *Int J CARS* **16**, 1015–1025 (2021). https://doi.org/10.1007/s11548-021-02385-2

Session III: Magnetic Nanoparticles: Synthesis & Functionalization

Synthesis and Characterisation of Superparamagnetic Iron Oxide Nanoparticle/β-Galactosidase bionanohybrid system for biomedical applications

Semi Hamzacebioglu, Harini Kopalle, and Maryam Weil

Faculty of Medical Engineering and Technomathematics,
FH Aachen University of Applied Sciences, Campus Jülich,
D-52428 Jülich, Germany

E-Mail: semi.hamzacebioglu@alumni.fh-aachen.de
Web: www.fh-aachen.de

Abstract – The subject of magnetically separable carriers for biomolecules, including enzymes, has attracted considerable interest in a variety of biomedical, bioanalytical and biotechnological contexts. The combination of enzymes with magnetic carriers provides the catalytic function of enzymes with external controllability and the potential for reuse [1]. Superparamagnetic iron oxide nanoparticles (SPIONs) are particularly well-suited for this purpose due to their size, magnetic separability, functionalizable surface, and biocompatibility.

In the present study, SPION/ligand/β-galactosidase bionanohybrids were systematically evaluated as a model platform for magnetically responsive enzymatic systems. The present study focused on comparing the synthesis, coating, biofunctionalization, washing, and UV–Vis spectroscopic readout protocols to identify process steps related to detectable enzymatic activity. SPIONs were synthesized by co-precipitation of Fe^{2+} and Fe^{3+} ions from iron(II) chloride and iron(III) chloride. In an inert atmosphere, ammonia was added dropwise to precipitate magnetite, followed by heating at 80°C, magnetic washing, pH adjustment, and ultrasonic deagglomeration [2].

A comprehensive characterization of the nanoparticles was conducted, which enabled the measurement of the magnetic core diameter using frequency-mixing magnetic detection (FMMD), the physical particle diameter as observed through scanning electron microscopy (SEM), and the hydrodynamic diameter determined by dynamic light scattering (DLS). Subsequently, the synthesized SPIONs were divided into two groups. One group was coated with polyethylene glycol (PEG), while the other was modified with ethylenediaminetetraacetic acid (EDTA). Then, the nanoparticles in both groups were functionalized and incubated with the enzyme β-galactosidase [3]. Following the completion of the incubation process, the unbound enzyme was removed through a series of four washing steps. The enzymatic activity of the resulting bionanohybrids was evaluated at 37°C using o-nitrophenyl-β-D-galactopyranoside (ONPG) as the substrate. The formation of o-nitrophenol was monitored spectrophotometrically at 420 nm using UV–Vis spectroscopy (Fig 1 a).

Characterization measurements demonstrated a magnetic core diameter of approximately 22 nanometers, as determined by FMMD detection method, and physical particle diameters of approximately 25 - 40 nm, as measured by SEM. DLS measurements showed hydrodynamic diameters of 66 -153 nm for uncoated SPIONs and 68 - 154 nm after PEG coating. In contrast, EDTA-coated particles exhibited markedly larger diameters of 1552 - 7265 nm, indicating pronounced aggregation.

As demonstrated in Figure 1b, the UV-Vis spectra of the bionanohybrid system, prepared without ultrasonic treatment following particle coating, exhibit distinct characteristics. The EDTA-based bionanohybrid demonstrated a distinct peak in its absorption spectrum at approximately 420 nm,

thereby confirming the formation of o-nitrophenol and, consequently, the enzymatic activity of immobilized β-galactosidase. The mean value of the degree of absorption decreased from 1.39 a.u. during the initial measurement to 0.90 a.u. following the second measurement. This finding suggests that the immobilized enzyme retained its activity even after the removal of unbound or weakly bound enzyme. Conversely, Figure 1c illustrates an EDTA-based bionanohybrid system that was exposed to repeated ultrasonic treatment following particle coating and prior to enzyme immobilization. In this instance, the absence of a characteristic peak at approximately 420 nm was observed, indicating the non-existence of quantifiable enzymatic activity. In summary, the decline in observable activity was found to be associated with the implementation of repeated ultrasonication following the process of particle coating.

The results demonstrate that electrostatic immobilization can result in a stable and reusable SPION/enzyme system (Fig 1b), as evidenced by the sustained enzymatic activity after repeated magnetic separation and storage. However, the observed loss of activity (Fig 1c) following ultrasonication after ligand functionalization as well as enzyme immobilization indicates that the system is sensitive to process-induced mechanical stress. Subsequent studies should directly compare identically coated nanoparticles processed with and without ultrasonication and quantify ligand and enzyme loading using Fourier-transform infrared (FTIR) spectroscopy.

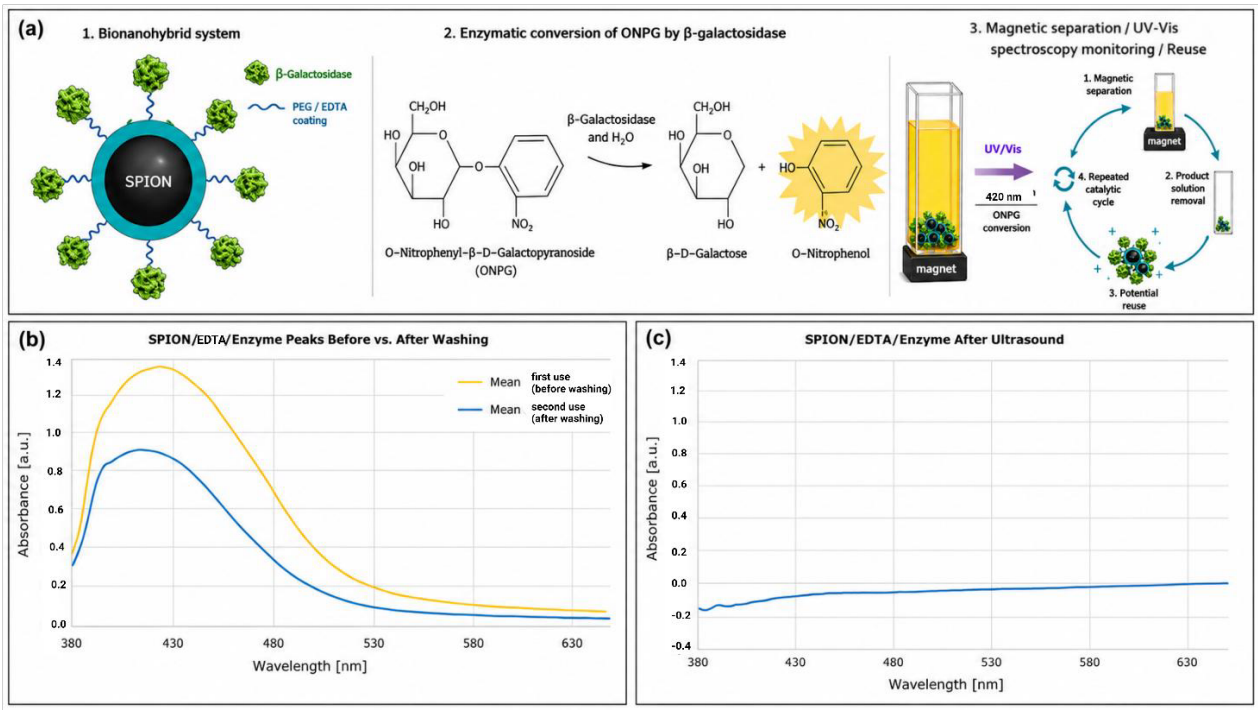

Fig. 1: *(a) SPION-based bionanohybrid system, ONPG conversion, and magnetic recovery and reuse concept; (b) UV–Vis spectra before and after washing for the functional reference system (without ultrasonic deagglomeration after coating); and (c) UV–Vis spectrum after ultrasonic treatment. treatment.*

Acknowledgment: The authors are profoundly grateful to Professors Hans-Joachim Krause and Ulrich Engelmann for their invaluable support with the FMMD and DLS measurements, respectively, which were instrumental in the realization of this study.

References

[1] S. Anboo et al., “Recent advancements in enzyme-incorporated nanomaterials: Synthesis, mechanistic formation, and applications,” *Biotechnology and Bioengineering*, vol. 119, no. 10, pp. 2609–2638, 2022.

[2] A. Ali et al., “Review on Recent Progress in Magnetic Nanoparticles: Synthesis, Characterization, and Diverse Applications,” *Frontiers in Chemistry*, vol. 9, article 629054, 2021.

[3] V. D. Nguyen et al., “Immobilization of β-galactosidase on chitosan-coated magnetic nanoparticles and its application for synthesis of lactulose-based galactooligosaccharides,” *Process Biochemistry*, vol. 84, pp. 30–38, 2019.

Session IV: Biomaterials & Tissue Engineering

Diameter-Dependent Fabrication and Mechanical Assessment of Layer-by-Layer Silk Fibroin Vascular Grafts Prototypes

Chorouk Dya[1,2], Maike Bittner[2,3], Benedetta Isella[2] and Ilya Digel [1]

[1] Institute for Bioengineering,
FH Aachen University of Applied Sciences,
Heinrich-Mussmann-Str. 1, 52428 Jülich, Germany

[2] Fibrothelium GmbH,
Research and Development,
Philipstr. 8, Aachen, Germany

(3) School of Engineering and Institute for Health Discovery and Innovation,
University of Galway,
University Road, Galway, Ireland

E-Mail: chorouk.dya@fibrothelium.com
Web: www.fibrothelium.com

Abstract

Vascular grafts represent an important therapeutic approach for the treatment of cardiovascular diseases by enabling the replacement or reconstruction of damaged blood vessels [1]. The mechanical and clinical requirements as well as the overall performance of the grafts are however highly dependent on the dimensions of the vessels themselves. Indeed, for large (>8 mm diameter) and medium-size (6-8 mm in diameter) vessels, synthetic grafts have shown successful clinical performance despite being permanent devices and therefore presenting the possibility of developing long-term side effects [2,3]. On the other hand, grafts for the reconstruction of small-diameter vessels (1-6 mm) are currently not present on the market despite representing an unmet need [4,2]. Therefore, the development and evaluation of vascular grafts with different diameters is essential to investigate their specific mechanical requirements and suitability for vascular applications.

Silk fibroin has attracted increasing interest as a promising biomaterial due to its excellent biocompatibility, low toxicity, and favourable mechanical properties. Its combination of biological compatibility and mechanical stability makes it a potential candidate for vascular applications, where graft materials must withstand physiological forces while maintaining compatibility with the surrounding biological environment.

A layer-by-layer dip-coating process previously developed by [Isella et al] [5]. enables the fabrication of stand-alone tubular structures by depositing multiple layers onto a cylindrical substrate, which is removed after fabrication.

In this study, grafts with diameters of 2 mm, 4 mm, and 8 mm were fabricated to investigate the influence of substrate diameter on layer formation, resulting wall thickness, and mechanical performance. Burst pressure testing, tensile testing, and suture retention strength measurements were performed to assess their mechanical properties based on ISO 7198 [6].

This study therefore aims to determine whether the layer-by-layer silk fibroin fabrication process can be transferred across different graft diameters and how diameter-dependent structural properties affect the mechanical suitability of the resulting tubular grafts.

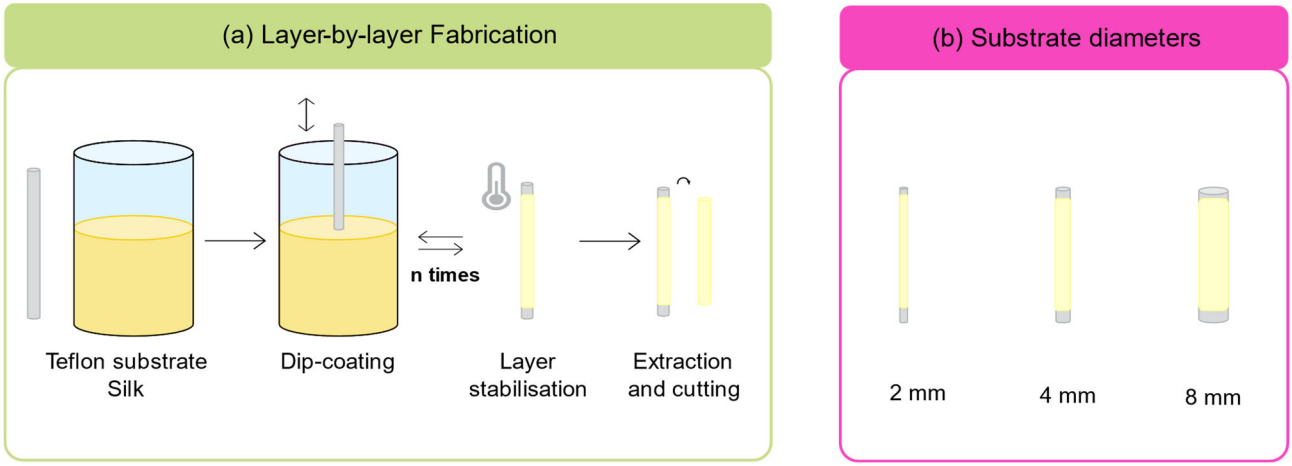

Fig. 1: (a) Silk fibroin multilayer coating process via dip coating, (b) Diameter variation of vascular graft substrates used in this study.

References

[1] K. K. Das, R. M. Tiwari, O. Shankar, P. Maiti, and A. K. Dubey, "Tissue-engineered vascular grafts for cardiovascular disease management: Current strategies, challenges, and future perspectives," *MedComm - ; Biomaterials and Applications*, vol. 3, no. 3, p. e88, Sep. 2024, doi: 10.1002/mba2.88.

[2] L. Bačáková *et al.*, "Vascular Damage and Repair - Are Small-Diameter Vascular Grafts Still the 'Holy Grail' of Tissue Engineering?," *Physiol Res*, no. Suppl 1, pp. S335–S363, Aug. 2024, doi: 10.33549/physiolres.935294.

[3] J. Chen, D. Zhang, L.-P. Wu, and M. Zhao, "Current Strategies for Engineered Vascular Grafts and Vascularized Tissue Engineering," *Polymers*, vol. 15, no. 9, p. 2015, Apr. 2023, doi: 10.3390/polym15092015.

[4] D. Liu *et al.*, "Evaluation of mechanical properties and biocompatibility of three-layer PCL/PLLA small-diameter vascular graft with pore diameter gradient," *European Polymer Journal*, vol. 186, p. 111864, Mar. 2023, doi: 10.1016/j.eurpolymj.2023.111864.

[5] B. Isella, *Development, Production, and Prediction of Fibroin-Based Degradable Implants*, Ph.D. dissertation, University of Galway, Galway, Ireland, 2024.

[6] Cardiovascular implants and extracorporeal systems — Vascular prostheses — Tubular vascular grafts and vascular patches, ISO 7198:2016, Geneva, Switzerland., 2016.

Dip-Coating of Silk Fibroin Tubular Structures for Microvascular Applications: A Parametric Study

Peace Oduyebo[1] [2], Mariana Rodrigues[2] [3], Benedetta Isella[2] and Ilya Digel[1]

[1] Institute for Bioengineering,
Aachen University of Applied Sciences,
Heinrich-Mußmann-Str. 1, 52428 Jülich, Germany

[2] Fibrothelium GmbH,
Research and Development,
Phillipstr. 8, Aachen, Germany
E-Mail: info@fibrothelium.com
Web: www.fibrothelium.com

[3] Department for Biohybrid & Medical Textiles (BioTex),
AME - Helmholtz Institute for Biomedical Engineering,
RWTH Aachen University, Germany

Abstract
Small-diameter vascular grafts (SDVGs, inner diameter ≤ 6 mm) remain a major challenge in cardiovascular surgery due to their high failure rates. Currently available SDVGs often exhibit poor long-term biocompatibility and an increased risk of thrombosis, which significantly limits their clinical applicability. These limitations are largely attributed to the inability of conventional synthetic materials to adapt to the physiological environment, resulting in graft occlusion and loss of patency [1]. To overcome these challenges, natural biomaterials such as silk have gained increasing attention [2]. Silk fibroin, the primary structural protein of *Bombyx mori* silk, can be processed into a range of biomedical products, including tubular scaffolds [3], and its combination of hemocompatibility, mechanical robustness and ready availability make silk fibroin well suited for vascular applications such as small-diameter grafts and anastomotic devices [4], [5], [6]. The overall fabrication workflow, stabilization setups, and mechanical testing configuration are illustrated in Fig. 1.
This study investigates the fabrication of silk fibroin tubular structures using a dip-coating process and systematically evaluates the influence of key process parameters, namely stabilization setup (open and closed), stabilization time (30 and 60 minutes), and number of coated layers (6, 8, and 10) on their resulting structural and mechanical properties. The closed stabilization setup (60 min, 10 layers) represents an established fabrication protocol at Fibrothelium GmbH [7] and was used as a baseline, while the open setup was systematically varied to explore process optimization using a one-factor-at-a-time (OFAT) approach.
The results demonstrate that the open stabilization setup produces tubular structures with increased wall thickness, from 192.29 ± 7.16 µm to 257.84 ± 11.83 µm at 10 layers with a stabilisation time of 60 minutes. This change in setup also led to an increase in ultimate tensile strength (UTS) and burst pressure (BP) compared to the established closed system. Stabilization time showed no significant influence on UTS and BP, it did however minimally influence the wall thickness of samples. As a process optimization step, in light of the difference in thickness, the influence of the number of coated layers on the performance of these constructs were investigated in subsequent experiments. Variations in layer number showed no significant effect on UTS and Young's Modulus, whereas BP decreased with a reduction in layer number, with a pronounced drop from 10 to 8 layers and a less substantial decrease from 8 to 6 layers.
Overall, this study highlights the importance of process parameter optimization in tailoring the mechanical performance of silk fibroin tubular structures. The findings contribute to the development of mechanically stable and surgically reliable small-diameter vascular grafts with potential for improved clinical performance.

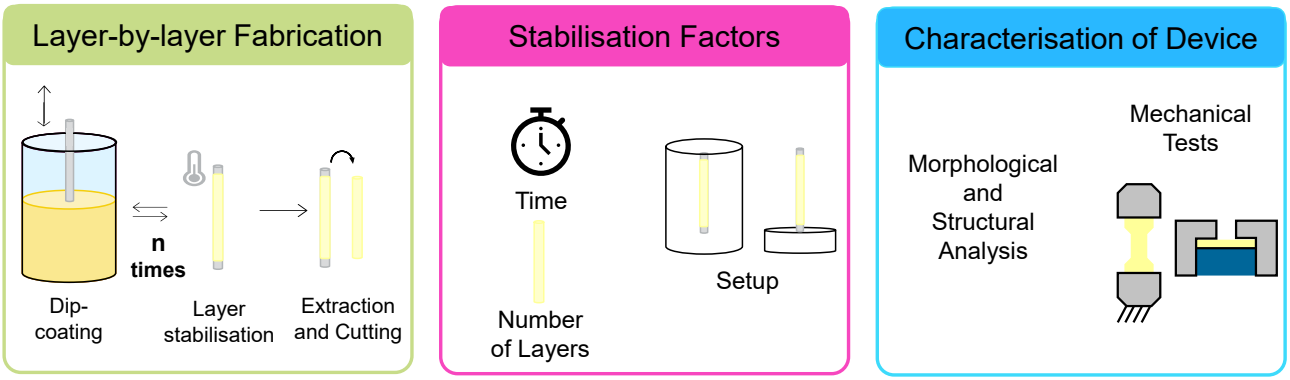

Fig. 1: a) Schematic of the layer-by-layer dip-coating process for silk fibroin tubular structures; (b) stabilisation factors; (c) mechanical testing configuration

References

[1] S. Pashneh-Tala, S. MacNeil, and F. Claeyssens, "The tissue-engineered vascular graft - Past, present, and future," *Tissue Eng. Part B Rev.*, vol. 22, no. 1, pp. 68–100, 2016, doi: 10.1089/ten.teb.2015.0100.

[2] K. K. Das, R. M. Tiwari, O. Shankar, P. Maiti, and A. K. Dubey, "Tissue-engineered vascular grafts for cardiovascular disease management: Current strategies, challenges, and future perspectives," *MedComm - Biomaterials and Applications*, vol. 3, no. 3, pp. 1–40, 2024, doi: 10.1002/mba2.88.

[3] V. Murugesan, S. Mundada, and S. Rajagopal, "Silk fibroin as a functional biomaterial for tissue engineering," *Silk Fibroin: Advances in Applications and Research*, vol. 22, pp. 155–175, 2023, doi: 10.3390/ijms2.

[4] C. Vepari and D. L. Kaplan, "Silk as a biomaterial," *Progress in Polymer Science (Oxford)*, vol. 32, no. 8–9, pp. 991–1007, 2007, doi: 10.1016/j.progpolymsci.2007.05.013.

[5] R. R. Jose *et al.*, "Rapid prototyped sutureless anastomosis device from self-curing silk bio-ink," *J Biomed Mater Res Part B: Appl Biomater*, vol. 103, pp. 1333–1343, 2014, doi: 10.1002/jbm.b.33312.

[6] D. Wang, H. Liu, and Y. Fan, "Silk fibroin for vascular regeneration," *Microsc. Res. Tech.*, vol. 80, no. 3, pp. 280–290, 2017, doi: 10.1002/jemt.22532.

[7] B. Isella, T. J. Vaughan, and A. Kopp, "Development, Production, and Prediction of Fibroin-Based Degradable Implants," Doctoral thesis, University of Galway, 2024. doi: https://doi.org/10.13025/29130.

Parameter and Morphology Analysis of Electrospun Silk Fibroin Membranes for Guided Bone Regeneration

Robin Schlinkmann[(1)] and Thomas Gries[(1)]

[(1)] ITA – Institut für Textiltechnik
RWTH Aachen University
52074 Aachen, Germany
E-Mail: robin.schlinkmann@ita.rwth-aachen.de

Web: www.ita.rwth-aachen.de/go/id/jezh/

Abstract – Electrospinning of silk fibroin has attracted increasing attention for biomedical membrane applications due to its biocompatibility, biodegradability, and structural similarity to extracellular matrix architectures. For guided bone regeneration (GBR) membranes, structural parameters such as fiber diameter, pore architecture, thickness, and reproducibility of fabrication are critical, as they determine barrier function, permeability, and mechanical stability [1]. However, stable electrospinning of aqueous silk fibroin solutions remains challenging, particularly at lower concentrations, where jet instabilities and bead formation frequently occur [2].
The present study aims to define a reproducible electrospinning process window for concentrated silk fibroin solutions and to establish clear process–structure relationships relevant for membrane fabrication.

Aqueous silk fibroin solutions with concentrations ≥25 wt% were investigated. Preliminary trials showed that stable electrospinning could only be achieved above a critical concentration threshold. Solutions were concentrated via controlled heating to enable stable jet formation.
A standardized 27 wt% fibroin solution was selected for systematic investigations. A one-factor-at-a-time (OFAT) approach was applied to isolate the influence of key electrospinning parameters, including applied voltage, flow rate, and needle-to-collector distance. Environmental conditions were controlled to ensure process stability.
Fiber morphology was analyzed via light microscopy and scanning electron microscopy (SEM). Mean fiber diameters were determined from micrographs. Membrane thickness was adjusted by varying spinning time and measured using thickness analysis across defined sample regions.

Stable and continuous fiber formation was only achievable at fibroin concentrations ≥25 wt%, confirming the existence of a critical concentration required for process stability. Below this threshold, jet breakup, droplet formation, and irregular deposition were observed.
Using the standardized 27 wt% solution and optimized parameter settings, uniform nonwoven membranes were reproducibly fabricated. Mean fiber diameters of approximately 2.5 µm were achieved. This diameter range lies within the microfibrous regime and enables mechanically stable nonwoven structures with interconnected pore architecture.
Membrane thickness could be precisely adjusted by controlling spinning time. Thin membranes exhibited average thicknesses of 0.13–0.16 mm, while extended deposition resulted in thicker variants up to 0.37 mm. Thickness scaled consistently with deposition time, demonstrating controlled material build-up.
SEM analysis confirmed homogeneous fiber morphology with well-defined, straight fibers and an open, interconnected pore structure. The resulting architecture provides structural integrity while maintaining permeability—characteristics essential for membrane-based biomedical applications such as GBR.

This study establishes a defined electrospinning process window for concentrated silk fibroin solutions and demonstrates clear process–structure relationships governing microfiber formation and

membrane build-up. A critical concentration threshold was identified as a key factor for stable jet formation and reproducible membrane fabrication.
The achieved microfibrous architecture (mean diameter ~2.5 µm) enables a balanced combination of mechanical stability, controlled thickness, and open pore structure. These findings highlight the importance of concentration-driven process stabilization in silk fibroin electrospinning and provide a reproducible framework for the fabrication of structurally tunable membranes for biomedical applications.

References

[1] Kwon, K.-J.; Seok, H. Silk protein-based membrane for guided bone regeneration. *Applied Sciences*, 2018, 8, 1214.

[2] Cai, Y. et al. Silk fibroin membrane used for guided bone tissue regeneration. *Materials Science and Engineering,* 2017, 70, 148–154.

Session V: Phantoms, Materials & Preclinical Testing

Hydrogel Tissue Phantoms for Mimicking Electrical Properties in Laboratory Setups for Preclinical Evaluation

Johannes Brüning, Monika Kolodziej, Thomas Hilbel, and Michael Schlüter

Westphalian University of applied Science
Department for Electrical Engineering and Applied Sciences
45897, Gelsenkirchen, Germany

E-Mail: johannes.bruening@w-hs.de
Web: www.w-hs.de

Abstract – Electrical-property-based diagnostic principles are widely investigated in medical research and the development of medical devices. Prominent examples include impedance plethysmography, biomarker quantification via impedance spectroscopy, and reduced-lead electrocardiography. These approaches demonstrate strong potential for implementation in wearable systems and devices for continuous patient monitoring. [1–3]

However, in the development phase prior to clinical trials, reproducible evaluation remains challenging. One previously explored approach involves the use of hydrogel-based laboratory setups to mimic the electrical behaviour of human tissues during measurement procedures [4, 5].
Building upon previous work, this study further develops tissue phantom manufacturing techniques. The materials employed include phosphate-buffered saline solution, sodium chloride, glycerin, agar, and gelatin. By adjusting the composition, the electrical properties of skin, muscle, and fat tissue can be approximated. The manufacturing process is illustrated in Fig. 1A. By using segmented pouring and cooling with controlled timing and temperature, layered tissue structures can be formed, which facilitates representative measurement scenarios (Fig. 1B).

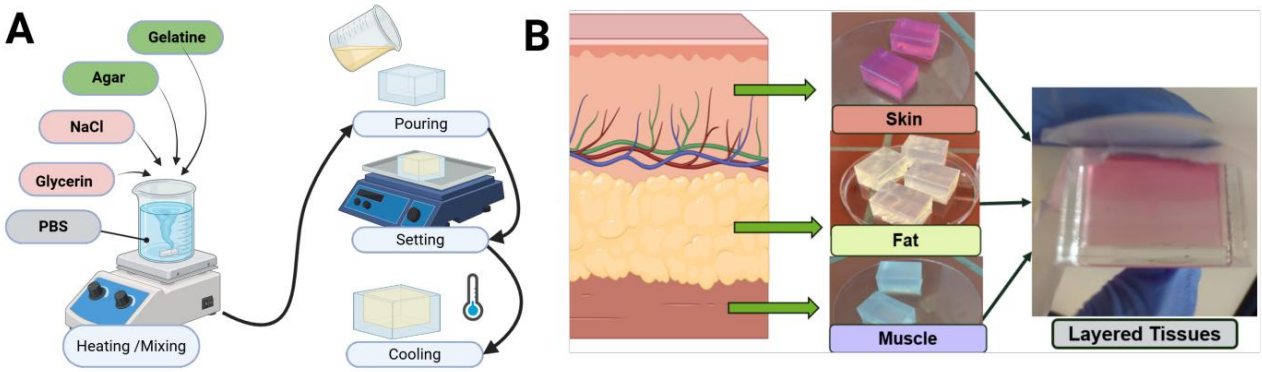

Fig.1: A: Schematic representation of the hydrogel phantom manufacturing pipeline. B: Examples of fabricated individual and combined tissue phantoms.

A key aspect of the fabrication process is the use of custom moulds made from polydimethylsiloxane (PDMS), which allow controlled extraction due to their hydrophobic properties and enable micropatterning of the contact surface. Imprinted surface structures were characterized using confocal microscopy (Nanofocus). The resulting topography exhibits height variations on the order of approximately 150 µm, comparable to human skin, leading to similar electrode–tissue contact behaviour. [6]

The electrical properties were evaluated using electrochemical impedance spectroscopy (EIS Reader K-U, CGS Sensors GmbH) over a frequency range from 50 kHz to 100 MHz. To validate the results, the individual tissue phantoms were compared to a passive electrical tissue database built on the work of Gabriel et al. [7]. A strong correlation with reference data was observed, exceeding r = 0.9 up to frequencies of approximately 5 MHz, with increasing deviations at higher frequencies. Under reproducible conditions, the variability of measurements remained below the innate error margin of the measurement device. However, factors such as temperature and phantom age were found to influence the electrical properties.
Ongoing developments are centred around the inclusion of fluid channels in the tissue phantoms.

Availability of Resources: Upon request, we are happy to provide detailed manufacturing protocols and material specifications, which are not included here due to space limitations.

Acknowledgement: The authors would like to thank the Westphalian University of Applied Sciences for funding this research independently. Furthermore, we acknowledge the support of our research assistants, Ozan Divli and Viktoria Luft genannt Plaisier, in laboratory work.

References

[1] S.-H. Liu, D.-C. Cheng, and C.-H. Su, “A Cuffless Blood Pressure Measurement Based on the Impedance Plethysmography Technique,” *Sensors (Basel)*, vol. 17, no. 5, p. 1176, May 2017.

[2] Q. Gong et al., “Non-Invasive and Accurate Blood Glucose Detection Based on an Equivalent Bioimpedance Spectrum,” *Appl. Sci.,* vol. 15, no. 3, Art. no. 3, Jan. 2025

[3] R. Mieloszyk et al., “A Comparison of Wearable Tonometry, Photoplethysmography, and Electrocardiography for Cuffless Measurement of Blood Pressure in an Ambulatory Setting,” *IEEE J. Biomed. Health Inform.*, vol. 26, no. 7, pp. 2864–2875, Jul. 2022.

[4] Y. Yu, A. Lowe, G. Anand, and A. Kalra, “Tissue phantom to mimic the dielectric properties of human muscle within 20 Hz and 100 kHz for biopotential sensing applications,” in Proc. *41st Annu. Int. Conf. IEEE Eng. Med. Biol. Soc. (EMBC)*, Jul. 2019, pp. 6490–6493.

[5] G. Anand, A. Lowe, and A. Al-Jumaily, “Tissue phantoms to mimic the dielectric properties of human forearm section for multi-frequency bioimpedance analysis at low frequencies,” *Mater. Sci. Eng. C,* vol. 96, pp. 496–508, Mar. 2019.

[6] A. Lo Presti et al., “Fundamentals of Skin Bioimpedances,” *Adv. Mater.*, vol. 35, no. 33, p. 2302127, 2023.

[7] D. Andreuccetti, R. Fossi, and C. Petrucci, “An Internet resource for the calculation of the dielectric properties of body tissues in the frequency range 10 Hz–100 GHz,” *IFAC-CNR*, Florence, Italy, 1997. [Online]. Available: http://niremf.ifac.cnr.it/tissprop

Preliminary Study on the Suitability of PDMS as a Material for Target Transfer Lines

Tim C. Wichmann[(1)], Johannes Brüning[(2)], Michael Schlüter[(2)] and Michael Nader[(1)]

[(1)] Department of Nuclear Medicine, Division of Radiopharmacy
Faculty of Medicine, University Duisburg-Essen
D-45147 Essen, Germany

[(2)] Lab for Microsystems Technology
Faculty of Physical Engineering, Westphalian University of Applied Sciences
D-45897 Gelsenkirchen, Germany

E-Mail: Tim.Wichmann@stud.uni-due.de
Web: https://nuklearmedizin.uk-essen.de

Abstract – In radiopharmaceutical production, the transfer of radioactive material from its source to the synthesis module represents a critical process step. This transfer is performed through narrow tubing with lengths ranging from 10 m to 30 m. The tubing typically has a standard inner diameter of 0.762 mm and differs primarily in material composition. The selection of the most suitable tubing material remains an ongoing topic of discussion [1]. Currently, PEEK and ETFE are the most widely used materials, each of which exhibits distinct advantages and limitations for this application.
To identify an alternative transferline material, this study evaluates PDMS. Due to its widespread use in radiopharmaceutical development, low flow resistance [2], chemical inertness [3], and high radiation resistance [4], it represents a promising candidate for transfer-line applications. In addition, its fluorine-free composition eliminates the risk of contamination with non-radioactive ^{19}F.
To allow a direct comparison between the different materials, a PDMS channel (761 ± 65 µm) with comparable geometry to the selected PEEK tubing (762 ± 25 µm) was manufactured using the ESCARGOT procedure [5], employing ABS as sacrificial scaffold.

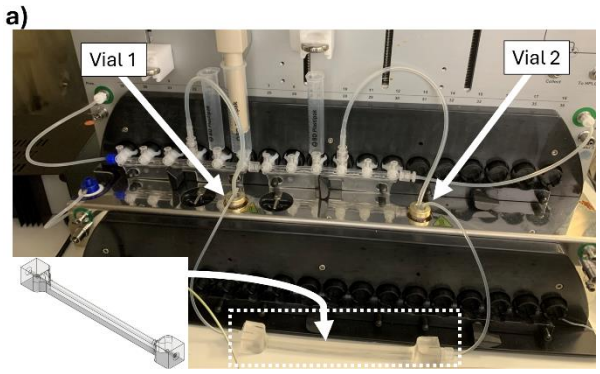

Fig.1: a) Measurement setup with the PDMS channel illustrated.

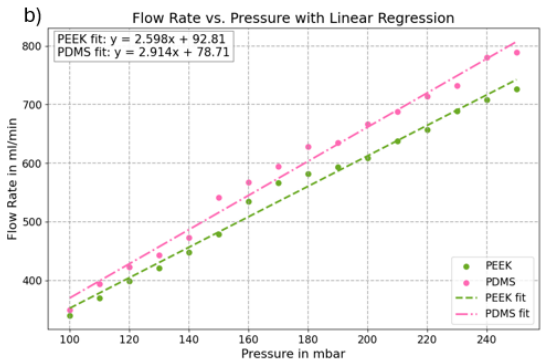

b) N2 Flow comparison between PEEK and PDMS channels

The test tubing was integrated in a custom designed cassette installed into a Trasis All-In-One synthesis module, as shown in Figure 1a.
Using N_2 gas as the driving force, radioactive [^{18}F]/[^{18}O]-enriched water generated by a particle accelerator was transferred between the two vials through the marked test tubing. After each transfer cycle, the radioactivity in both vials was measured to determine the transfer efficiency and evaluate the overall performance of the tubing material, as shown in Figure 2.

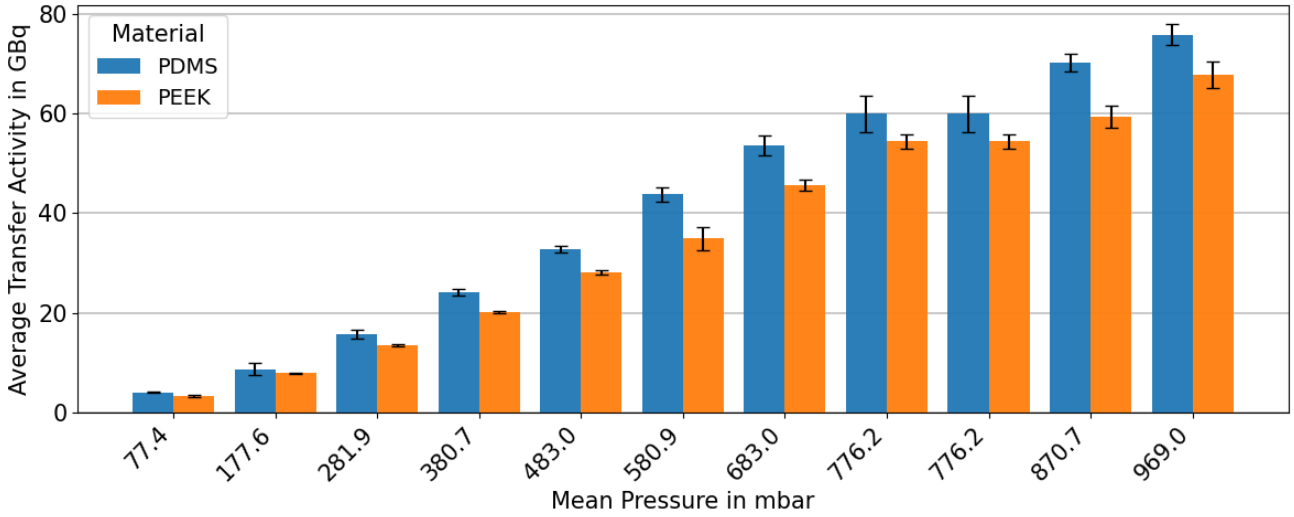

Fig.2: Comparison of radioactive transfer through PEEK and PDMS under different pressure conditions.

Each column in Figure 2 represents the average activity of 3 mL of radioactive material transferred from Vial 1 to Vial 2 within 30 seconds over 20 transfer cycles for PEEK and PDMS tubing at different pressure levels. The different pressure levels simulate successive transfer-line segments, as the pressure typically decreases along the transfer path due to hydraulic resistance. Even in this simplified experimental setup, a clear difference in transfer performance between PDMS and PEEK is observed across all investigated pressure levels and, consequently, throughout all simulated line segments. These findings are further supported by the conventional flow-resistance measurements shown in Figure 1b. The lower flow rates measured for PEEK at identical N_2 pressures indicate a higher fluidic resistance compared to PDMS tubing. The results suggest that PDMS could be a promising material for target-transfer lines. Although these initial experiments demonstrate promising performance, previous studies have reported potential degradation of PDMS in ^{18}F applications [3]. Further investigations are therefore required to evaluate the long-term stability of PDMS tubing in larger-scale systems and under continuous operation in a production environment.

References

[1] International Atomic Energy Agency, ”Production and Quality Control of Fluorine-18 Labelled Radiopharmaceuticals”, *INTERNATIONAL ATOMIC ENERGY AGENCY VIENNA,* 2021 IAEATECDOC-1968 pp. 22.

[2] Ines Ramos, et. al. ”PDMS surface wettability modification and its applications: A systematic review”, *Journal of Molecular Liquids,* 434, (2025), 127978

[3] A.Mc Veigh, et. al. ”Understanding the Compatibility of Fluoride-Based Radiopharmaceutical Reaction Solutions and PDMS”, doi:10.1021/acsami.5c21729

[4] Tereza-Markéta Durďáková et. al., ”Radiation softening and hardening of PDMS in combined neutron and Gamma rays”, *Polymer Degradation and Stability*, vol. 208 (2023), 110241

[5] V. Saggiomo and A. H. Velders, ‘Simple 3D Printed Scaffold-Removal Method for the Fabrication of Intricate Microfluidic Devices’, *Adv Sci* (Weinh), vol. 2, no. 9, p. 1500125, Jul. 2015, doi: 10.1002/advs.201500125

Session VI: Medical Devices, Robotics & Biomechanics

Design and implementation of a communication interface for cobot teleoperation with haptic feedback in ultrasound diagnostics

Timo Waschk(1), Soufian Benchaou(1), Carole Leguy(1) and Richard Lopata(2)

(1) Institute of measurement and sensor technology,
University of Applied Sciences Ruhr West,
D-45479 Mülheim, Germany

(2) Photoacoustics & Ultrasound Laboratory,
Department of Biomedical Engineering, Eindhoven University of Technology,
NL-5612 AE Eindhoven, Netherlands

E-Mail: timo.waschk@hs-ruhrwest.de
Web: www.hochschule-ruhr-west.de

Abstract – Teleoperation of robotic systems is becoming increasingly important in technical and medical applications, as the physical separation between the operator and the robotic system enables complex tasks to be carried out from a safe distance. In the medical field in particular, this opens up new possibilities for the flexible implementation of diagnostic and therapeutic procedures, whilst at the same time improving ergonomics and precision during operation [1, 2, 3]. One area of medicine in which robotics is used is ultrasound. In addition to providing imaging support during surgical interventions to reduce the amount of necessary personnel, routine examinations are particularly well suited as applications for robotic ultrasound systems. Among other things, the use of robotic systems enables the 3D reconstruction of blood vessels from 2D images, thereby expanding diagnostic capabilities [4].
This work addresses the following research questions to develop a teleoperated robotic ultrasound system:

- How can a low-latency and stable real-time teleoperation system be implemented using a 6D haptic interface and a collaborative robot in ultrasound diagnostics?
- What are the characteristics of the developed teleoperation architecture in terms of communication frequency, motion transmission and position scaling?
- How can force and torque feedback be integrated into the developed teleoperation architecture and investigated experimentally?

The proposed teleoperation system consists of a haptic input device and an industrial cobot, which has an ultrasound probe attached at the end-effector. The Haption Virtuose 6D (Haption SAS, France) serves as the master device and enables the user to specify position and orientation via a 6-DOF interface with force feedback. Position and orientation are transmitted via the User Datagram Protocol (UDP) to a control application. There, necessary processing steps – such as coordinate system transformation – are carried out, along with optional operations like upscaling or downscaling the recorded movement. The Universal Robots UR3e (Universal Robots, Denmark) is used as the slave system. This is a collaborative robot with 6 degrees of freedom that supports real-time Cartesian control of the tool centre point (TCP) and is controlled via the bi-directional Real-Time Data Exchange (RTDE) interface. The aim of the system is to map the user's hand movements, as detected by the haptic device, onto the robot's Cartesian workspace in real time, whilst simultaneously feeding back the forces exerted at the robot's TCP to the force feedback device.
The proposed system was evaluated by assessing the communication frequency, positional accuracy and force feedback accuracy. In order to evaluate the communication frequency, the actual control frequency was determined experimentally. For this purpose, a loop counter with time-based averaging was used at specified measurement intervals, whilst movements were performed using the haptic device and setpoint frequencies varied between 100 and 500 Hz. Position scaling was investigated by applying translational movements along the Cartesian X, Y and Z axes of 10, 20 and

30 cm, using a scaling factor of 0.1 to reduce the amount of movement from the robot. The measurement was repeated three times for every distance. For the analysis of force and torque feedback, the robot's force and torque sensor was first zeroed whilst unloaded; a vertically applied force was then measured at the TCP and compared with the theoretical weight force applied by the robot and the force that is fed back to the haptic device.

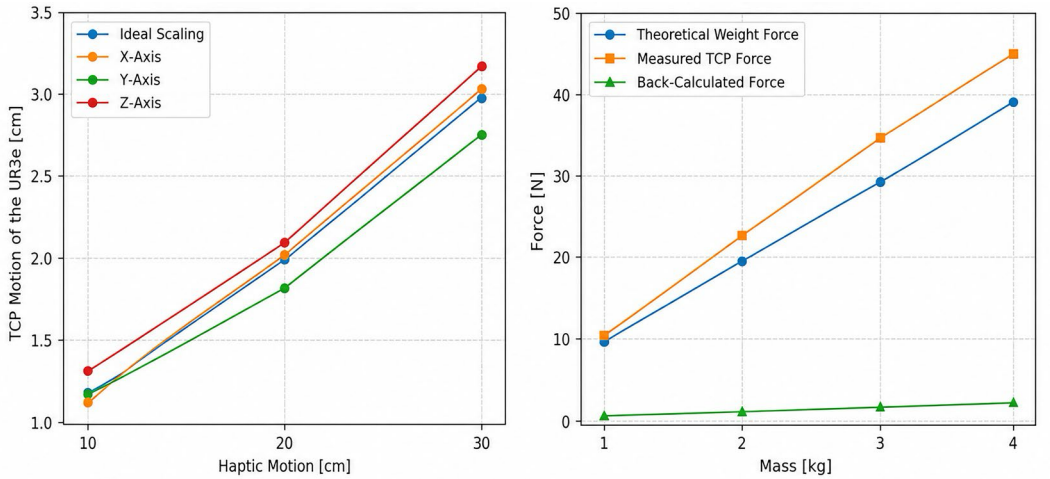

Fig.1: (a) Comparison of Cartesian motion of Virtuose 6D and UR3e for each axis (UR3e motion is scaled down by factor 0.1) and the ideal relation of motion. (b) Comparison of the theoretical weight force, the measured force at the TCP of the UR3e and the force fed back to the Virtuose 6D (fed back force is scaled down by factor 0.05).

An effective control frequency of around 100 Hz, which was maintained stably regardless of the setpoint frequency and enabled continuous, smooth teleoperation without interruptions or dropouts, was obtained. A comparison between the input motion and the robot motion actually achieved showed a reproducible transfer of the translational movements to the TCP of the UR3e. For all three Cartesian axes, the measured robot movements were close to the expected target values (see Fig.1). The deviations were particularly small along the x-axis. The slightly larger deviations along the y- and z-axes are likely due to a systematic error arising from the measurement setup. The forces measured were above the set target value (see Fig.1). This was presumably due to the measurement values being distorted by an elastic underlying surface. However, the signals were continuously read out, processed and transmitted to the haptic input device, so that the feedback forces were clearly perceptible.

Overall, the system demonstrates adequate performance for real-time teleoperation for medical ultrasound and shows potential for further optimization. The achieved communication frequency is sufficient for stable and smooth teleoperation. The positional accuracy and the force measurement need to be analysed further with better measurement setups and also together with an ultrasonic probe. Additionally, further analysis of system latency and stability of the orientation mapping under dynamic conditions is still required.

References

[1] Sheridan, T. B., Telerobotics, Automation, and Human Supervisory Control. Cambridge, MA, MIT Press, 1992.

[2] von Haxthausen, F., Böttger, S., Wulff, D., Hagenah, J., Garcia-Vazquez, V., Ipsen, S., " Medical Robotics for Ultrasound Imaging: Current Systems and Future Trends," *Current Robotics Reports, Vol. 2, No. 3,* pp. 193-205, *2021*

[3] Jiang, Z., Salcudean, S. E., Navab, N., "Robotic Ultrasound Imaging: State-of-the-Art and Future Perspectives", *Medical Image Analysis*, Vol. 85, Article 102754, 2023,.

[4] N. Petterson, M. Sjoerdsma, M. van Sambeek, F. van de Vosse, R. Lopata, " Mechanical characterization of abdominal aortas using multi-perspective ultrasound imaging," *Journal of the Mechanical Behavior of Biomedical Materials*, vol. 119, Article 104509, 2021.

Preoperative Reconstruction of Femoral Stem Geometry for Combined Target Zone Planning in Total Hip Arthroplasty

Mohammed Aouad[1], Luisa Berger[2], Klaus Radermacher[2], and Ilya Digel[1]

[1] Faculty of Medical Engineering and Technomathematics (FB09),
FH Aachen - University of Applied Sciences, Campus Jülich,
D-52428 Jülich, Germany

[2] mediTEC - Chair of Medical Engineering,
Helmholtz-Institute for Biomedical Engineering, RWTH Aachen University,
D-52074 Aachen, Germany

E-Mail: mohammed.aouad@alumni.fh-aachen.de

This work was conducted at mediTEC - Chair of Medical Engineering, Helmholtz-Institute for Biomedical Engineering, RWTH Aachen University.

Abstract – Total hip arthroplasty (THA) is one of the most common orthopedic procedures, and an implant's long-term outcome depends on accurate component placement. Suboptimal positioning is associated with prosthetic impingement, dislocation, leg-length discrepancy (LLD), and premature revision surgery [1]. Most planning work to date has focused on acetabular cup orientation, whereas planning of the femoral stem is comparatively less established. This work extends the Combined Target Zone (CTZ) concept, previously developed for the acetabular cup, to the femoral side. The aim is to reconstruct a planning-relevant femoral stem geometry from preoperative computed tomography (CT) data and to prepare the basis for a dedicated Stem Target Zone for patient-specific stem planning.
The CTZ framework introduced by Habor et al. [2] computes a safe zone for cup inclination and anteversion by intersecting a morphology-based target zone, derived from the patient's bone anatomy, with a range-of-motion (ROM)-based target zone derived from prosthetic impingement limits [3], [4]. On the femoral side, only a postoperative reference visualization was available, which shows the true implanted stem geometry directly from postoperative CT data but cannot be used for preoperative planning. The main challenge addressed here is to estimate the relevant femoral stem geometry from the preoperative femur mesh alone, without postoperative stem data or trochanteric landmarks.

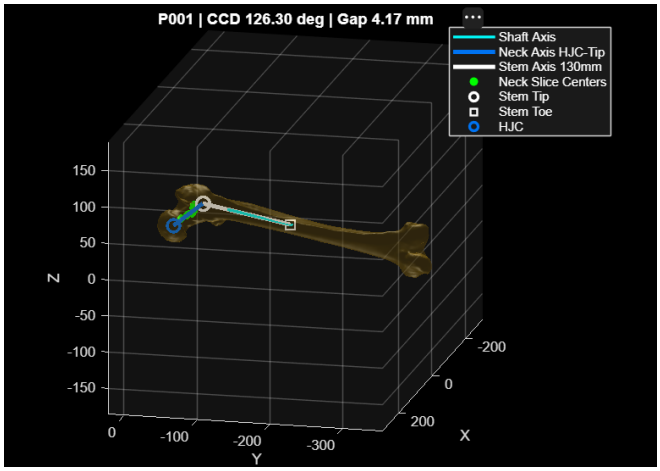

Figure 1: Reconstructed femoral stem geometry from preoperative data. Shaft axis (cyan), neck axis from HJC (blue), and stem axis (white). [@mediTEC, RWTH Aachen]

Method: The hip joint center (HJC) is obtained from the preoperative femur surface model using the *automaticFemoralCS* method [5] and serves as the proximal anatomical reference point for the reconstruction. The proposed stem-reconstruction method is then based on dedicated mesh-processing steps applied to the preoperative femur mesh and does not require postoperative stem data or trochanteric landmarks. First, the diaphyseal shaft axis is estimated from two shaft cross-sections by fitting a least-squares circle to each section and defining the axis as the line through the two circle centers. The femoral neck is then characterized by generating a series of cross-sections along an approximate HJC-to-shaft direction. For each section, the major, minor, and mean diameters are calculated. Sections corresponding to the femoral head or trochanteric region are identified by their larger diameters and discarded, and the neck axis is then defined by fitting a line through the centers of the remaining neck cross-sections using principal component analysis, anchored at the HJC (Fig. 1). Due to morphological variations, the calculated neck and shaft axes generally do not intersect in three-dimensional space. The intersection point is therefore estimated in three dimensions from the closest approach between the neck axis and the shaft axis, and the residual distance between both axes is retained as a geometric quality indicator. The stem toe is placed at a fixed stem length along the distal shaft direction. Finally, the prosthetic caput-collum-diaphyseal (CCD) angle is measured at the intersection point as the angle between the direction to the femoral head center and the direction to the stem toe. Building on this reconstruction, a virtual resection of the femoral neck is performed, and an interactive tool (Fig. 2) allows the CCD angle and the neck length to be varied to visualize their effect on femoral length and stem position. This provides a direct means of exploring the implant parameter space on a patient-specific basis and forms the basis for a future Stem Target Zone, in which valid CCD and neck-length combinations are determined systematically.

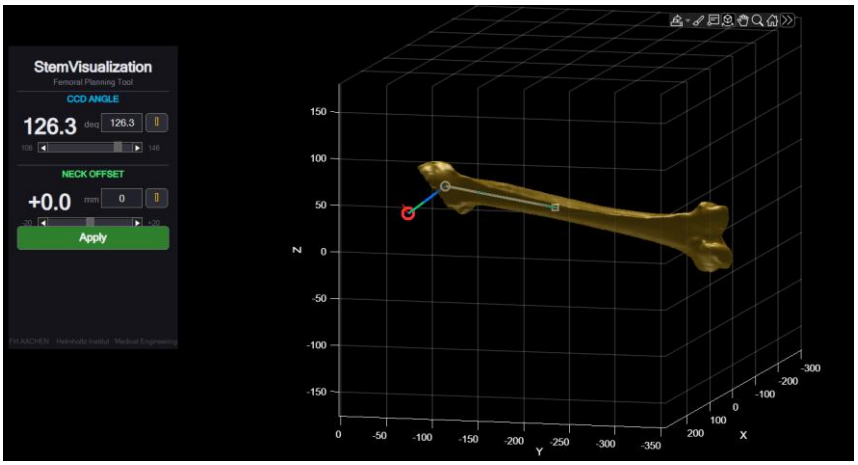

Figure 2: Interactive stem planning tool displaying the reconstructed shaft axis, neck axis, and stem axis on the preoperative femur. Sliders allow interactive adjustment of the CCD angle and neck offset. [@mediTEC, RWTH Aachen]

References

[1] G. E. Lewinnek, J. L. Lewis, R. Tarr, C. L. Compere, and J. R. Zimmerman, "Dislocations after total hip-replacement arthroplasties," *J. Bone Joint Surg. Am.*, vol. 60, no. 2, pp. 217–220, Mar. 1978.

[2] J. Habor, M. C. M. Fischer, K. Tokunaga, M. Okamoto, and K. Radermacher, "The patient-specific combined target zone for morpho-functional planning of total hip arthroplasty," *J. Pers. Med.*, vol. 11, no. 8, Art. no. 817, Aug. 2021, doi: 10.3390/jpm11080817.

[3] K.-H. Widmer and B. Zurfluh, "Compliant positioning of total hip components for optimal range of motion," *J. Orthop. Res.*, vol. 22, no. 4, pp. 815–821, Jul. 2004.

[4] F. Yoshimine, "The safe-zones for combined cup and neck anteversions that fulfill the essential range of motion and their optimum combination in total hip replacements," *J. Biomech.*, vol. 39, no. 7, pp. 1315–1323, 2006.

[5] M. C. M. Fischer, S. A. G. A. Grothues, J. Habor, M. de la Fuente, and K. Radermacher, "A robust method for automatic identification of femoral landmarks, axes, planes and bone coordinate systems using surface models," *Sci. Rep.*, vol. 10, Art. no. 20859, Nov. 2020, doi: 10.1038/s41598-020-77479-z.

Poster Sessions

Sustainable Green Synthesis of Magnetic Iron Oxide Nanoparticles

David Ayoub and Maryam Weil

Faculty of Medical Engineering and Technomathematics
FH Aachen University of Applied Sciences, Campus Jülich,
D-52428 Jülich, Germany
E-Mail: david.ayoub@alumni.fh-aachen.de
Web: www.fh-aachen.de

Abstract – Superparamagnetic iron oxide nanoparticles (SPIONs) are composed of magnetite (Fe_3O_4) or its oxidized form, maghemite (γ-Fe_2O_3), and exhibit a strong magnetic response that disappears once the external field is removed. This characteristic renders them suitable for a variety of biomedical and life-science applications, including MRI contrast enhancement, targeted drug delivery, magnetic hyperthermia in cancer therapy, and biosensing. This positions them as promising candidates for combined diagnostics and therapeutic applications [1]. Thus, their size, morphology, and crystallinity play a crucial role in these applications, which makes their production method a decisive factor.
Co-precipitation is the conventional synthesis method, frequently used alongside sol-gel processing, thermal decomposition, hydrothermal synthesis, and microemulsion routes. This procedure, which uses Fe^{2+}/Fe^{3+} salts under alkaline conditions, is the most established of these due to its simplicity and high yield. However, it typically relies on ammonia (NH_4OH), which is toxic and offers limited control over particle morphology. These drawbacks motivate a shift toward green synthesis, which replacing hazardous reagents with plant-derived alternatives that lower toxicity, reduce environmental impact, and simplify waste management under comparatively mild conditions [2].

Building on the conventional co-precipitation route, our approach replaces ammonia with sodium carbonate (Na_2CO_3) as the precipitating base, following the protocol of Patiño-Ruiz et al. (Sections 2.1–2.3) [3]. In this study, $FeCl_2$ and $FeCl_3$ are dissolved and stirred under a 0.2 bar N_2 atmosphere (700 rpm, 70 °C); Na_2CO_3 is then added stepwise in 10–15 mL portions at defined intervals (10 minutes), while stirring speed and temperature are adjusted (150 rpm, 80 °C) to promote controlled nucleation and particle growth [3].
Coating and stabilization are then achieved using an aqueous Moringa oleifera extract key phytochemicals molecules, which are ascorbic acid, gallic acid, and quercetin [4]. These compounds partially reduce Fe^{3+} to Fe^{2+}, helping establish the stoichiometry required for magnetite formation, while their hydroxyl and carboxyl groups adsorb onto the particle surface as a capping layer [4]. Ascorbic acid contributes strong electron-donating/antioxidant activity; gallic acid, a trihydroxybenzoic acid, combines reducing power with metal-chelating ability [5]; and quercetin, a flavonol, offers multiple phenolic binding sites [5]. Together, they are expected to influence final particle size, morphology, colloidal stability, and functional surface properties.

The resulting SPIONs will be characterized by UV-Vis spectrophotometry to confirm nanoparticle formation and monitor surface functionalization.

References

[1] T. C. De Souza, A. F. D. S. Costa, G. M. Vinhas, und L. A. Sarubbo, „Synthesis of Iron Oxides and Influence on Final Sizes and Distribution in Bacterial Cellulose Applications“, *Polymers*, Bd. 15, Nr. 15, S. 3284, Aug. 2023.
[2] S. Mohd. Waseem, S. V. Gaikwad, V. A. Pandit, und N. N. Kapse, „Iron Oxide Nanoparticles for Catalytic Applications: Synthesis, Characterization, and Environmental Performance“, *Top. Catal.*, Bd. 69, Nr. 8–11, S. 1337–1360, Apr. 2026.
[3] D. Patiño-Ruiz, L. Sánchez-Botero, L. Tejeda-Benitez, J. Hinestroza, und A. Herrera, „Green synthesis of iron oxide

nanoparticles using Cymbopogon citratus extract and sodium carbonate salt: Nanotoxicological considerations for potential environmental applications“, *Environ. Nanotechnol. Monit. Manag.*, Bd. 14, S. 100377, Dez. 2020.

[4] S. K. Begum *u. a.*, „Green synthesis of magnetite (Fe3O4) and hematite (Fe2O3) nanoparticles using Moringa oleifera and Psidium guajava leaf extracts for sustainable applications“, *Sci. Rep.*, Bd. 15, Nr. 1, S. 36465, Okt. 2025.

5] S. Eslami, M. A. Ebrahimzadeh, und P. Biparva, „Green synthesis of safe zero valent iron nanoparticles by *Myrtus communis* leaf extract as an effective agent for reducing excessive iron in iron-overloaded mice, a thalassemia model“, *RSC Adv.*, Bd. 8, Nr. 46, S. 26144–26155, 2018.

Magnetic Iron Oxide Nanoparticle-Based Enzyme Immobilization: A Comparative Kinetic Study

Edikan Okoko and Maryam Weil

Faculty of Medical Engineering and Technomathematics
FH Aachen University of Applied Sciences, Campus Jülich,
D-52428 Jülich, Germany
E-Mail: edikan.okoko@alumni.fh-aachen.de
Web: www.fh-aachen.de

Abstract – β-Galactosidase is a hydrolytic enzyme that catalyzes the conversion of lactose into glucose and galactose. This reaction is fundamental to lactose metabolism. Due to its well-characterized catalytic mechanism and straightforward activity assay, it is widely employed as a model enzyme for investigating performance and catalytic behaviour [1]. These characteristics provide it with broad industrial and biotechnological relevance, including in biosensor development [2], lactose-free food products [3], cancer research [4], enzyme-linked immunosorbent assays (ELISAs) [4] and prebiotic synthesis [5]. Despite its broad applicability, the use of free β-galactosidase is often limited by challenges associated with separation from the reaction medium, operational stability, and repeated reuse. Immobilization of the enzyme offers a strategy for overcoming these challenges with the potential trade-off of mass transfer limitations [6], steric hindrance [7] and conformational constraints [8] that may compromise catalytic performance.

The present study investigates this dynamic and whether any changes in enzyme behaviour are outweighed by improvements in enzyme reusability. The objective is to support more sustainable industrial and medical applications of β-galactosidase.

Among the available immobilization supports, superparamagnetic iron oxide nanoparticles (SPIONs) have attracted considerable interest owing to their superparamagnetism, high surface area-to-volume ratio, biocompatibility, environmentally friendly synthesis, and low toxicity [9]. Their unique magnetic properties enable magnetic separation of immobilized enzymes using an external magnetic field while maintaining a high surface area for enzyme loading, making them particularly attractive for reusable biocatalytic systems [9].

The effects of immobilization were evaluated by comparing the catalytic performance of immobilized β-galactosidase on polyethylene glycol (PEG)-functionalized SPIONs with that of the free enzyme. SPIONs were synthesized by co-precipitation, a simple, scalable, and environmentally compatible technique that has been widely employed for producing biocompatible iron oxide nanoparticles suitable for biomedical applications [9]. PEG is a well-known biocompatible polymer that improves colloidal stability through steric stabilization while providing a surface capable of physically adsorbing β-galactosidase via non-covalent interactions. The enzyme activity, kinetic behaviour, binding effectiveness, and operational stability were assessed by ultraviolet and visible light (UV–Vis) spectrophotometry. This was selected as the observation/measurement method as the hydrolysis of o-nitrophenyl-β-D-galactopyranoside (ONPG) by β-galactosidase yields the chromogenic product o-nitrophenol, which absorbs light waves of 420 nm [2]. This enabled quantitative monitoring of catalytic activity. In addition, the stability of the PEG-SPION/β-galactosidase nanobiohybrid was further evaluated after two months of storage to provide an initial indication of its longer-term stability.

The comparative evaluation of free and immobilized β-galactosidase provided insight into the effects of immobilization on catalytic performance and operational stability. The present study contributes to the understanding and characterization of enzyme immobilization systems. It provides a foundation for further optimization of said immobilization strategies involving SPION-based nanobiohybrid systems for biomedical applications.

References

[1] M. Kaur, A. Sood, G. S. Chauhan, and R. Gupta, "β-Galactosidase: a potential biotechnological enzyme," *Trends in Carbohydrate Research*, vol. 14, no. 4, pp. 26–39, 2023.

[2] S. Wei, Y. Dou, S. Song, and T. Li, “Functionalized-Graphene field effect transistor-based biosensor for ultrasensitive and label-free detection of β-galactosidase produced by Escherichia coli,” *Biosensors*, vol. 13, no. 10, Art. no. 925, 2023.

[3] S. Saqib, A. Akram, S.A. Halim, and R. Tassaduq, “Sources of β-galactosidase and its applications in food industry,” *3 Biotech*, May, vol. 7, no. 1, pp. 79, 2017.

[4] L. Liangliang, J. Feifei, L. Yunxiu, and P. Yan, “Design strategies and biological applications of β-galactosidase fluorescent sensor in ovarian cancer research and beyond,” *RSC Adv*, vol. 14, no. 5, pp. 3010–3023, 2024.

[5] M. A. Costa, C. Schmitz, J. C. de Lima, D. N. Lehn, and C. F. V. de Souza, “Recent perspectives on the biosynthesis of galacto-oligosaccharides: A systematic review and meta-analysis,” *Food Chemistry*, vol. 497, 2025.

[6] L. Andreas, and H. Lutz, “Evaluation of immobilized enzymes for industrial applications,” *Chem. Soc. Rev*, vol. 42, no.15, pp. 6236–6249, 2013.

[7] S. Francesco, “Conformational changes of enzymes upon immobilisation,” *Chem. Soc. Rev*, vol. 42, no. 15, pp. 6250–6261, 2013.

[8] R. C. Rafael, O. Claudia, Á. Berenguer-Murcia, T. Rodrigo, and R. Fernández-Lafuente, “Modifying enzyme activity and selectivity by immobilization,” *Chem. Soc. Rev*, vol. 42, no. 15, pp. 6290–6307, 2013.

[9] J. Wallyn, N. Anton, and T. E. Vandamme, "Synthesis, Principles, and Properties of Magnetite Nanoparticles for In Vivo Imaging Applications—A Review," *Pharmaceutics*, vol. 11, no. 11, Art. no. 601, 2019.

Towards a Sustainable Synthesis of Magnetic Iron Oxide Nanoparticles Through Process Optimization

Lisa Kissenkötter, David Ayoub and Maryam Weil

Faculty of Medical Engineering and Technomathematics,
FH Aachen University of Applied Sciences, Campus Jülich,
D-52428 Jülich, Germany
E-Mail: lisa.kissenkoetter@alumni.fh-aachen.de
Web: www.fh-aachen.de

Abstract – Superparamagnetic iron oxide nanoparticles (SPIONs) have attracted considerable attention in biomedical research due to their unique magnetic properties, biocompatibility, and a wide range of surface chemistry options. These characteristics render SPIONs promising candidates for a broad spectrum of biomedical applications, including magnetic resonance imaging, targeted drug and gene delivery, and magnetic hyperthermia [1–3].

This study focuses on the synthesis and comparison of SPIONs produced via two different synthesis pathways. Both SPION systems investigated in this work were synthesized using the co-precipitation method [4]. Iron oxides exist in various crystalline phases, each characterized by distinct crystal structures, oxidation states, and magnetic properties. Magnetic iron oxide nanoparticles refer to magnetite (Fe_3O_4) and maghemite (γ-Fe_2O_3), which exhibit superparamagnetic behavior at particle sizes below approximately 25 nm.

For the synthesis of both SPION systems, $FeCl_2$ and $FeCl_3$ precursor salts were used in a molar ratio of 1:2. The salts were dissolved in 100 mL of deionized water under an inert atmosphere to maintain the required stoichiometric ratio of Fe^{2+} to Fe^{3+} (Fig. 1a). In the subsequent synthesis step, a precipitating agent was added to provide hydroxide ions (OH^-), which react with the iron ions to form insoluble magnetic iron oxide nanoparticles (magnetite):

$$Fe^{2+} + 2Fe^{3+} + 8OH^- \rightarrow Fe_3O_4 + 4H_2O$$

The two synthesis pathways investigated in this study differ from this stage onward. In the conventional co-precipitation method, 30 mL of aqueous ammonia solution (NH_3(aq)) was added dropwise as the precipitating agent, followed by heating the suspension at 75–80 °C for 1 h. The hydroxide ions (OH^-) promote the precipitation of iron ions to form magnetite nanoparticles, as demonstrated below:

$$NH_3 + H_2O \rightleftharpoons NH_4^+ + OH^-$$

Ammonia solution is widely used as a precipitating agent in the co-precipitation synthesis of superparamagnetic iron oxide nanoparticles due to its high precipitation efficiency, good control over particle formation, and excellent reproducibility. However, its potential toxicity, volatility, and specific handling requirements raise environmental and safety concerns.

To improve the sustainability of the synthesis process, disodium carbonate (Na_2CO_3) was employed as an alternative precipitating agent in the second synthesis pathway. Compared with ammonia, Na_2CO_3 is less toxic, easier to handle, and has a lower environmental impact while providing sufficient alkalinity for the formation of magnetic iron oxide nanoparticles [5]. Thus, replacing ammonia with Na_2CO_3 represents a promising strategy for a more sustainable and environmentally friendly SPION synthesis. The following reactions show the formation of hydroxide ions from aqueous Na_2CO_3, enabling the coprecipitation of magnetic iron oxide nanoparticles.

$$Na_2CO_3 \rightarrow 2Na^+ + CO_3^{2-}$$

$$CO_3^{2-} + H_2O \rightleftharpoons HCO_3^- + OH^-$$

In the green synthesis pathway, 10 mL of disodium carbonate solution was added to the iron salt solution at 10-minute intervals over 1 hour while maintaining the reaction temperature at 70–75°C. The efficacy of the precipitation process was verified by the formation of a black, magnetic Fe_3O_4 precipitate (Fig. 1b). The nanoparticles were collected using an external magnet, washed five times with deionized water (Fig. 1c), ultrasonicated for 15 minutes to deagglomerate the SPIONs, and the pH was adjusted to improve colloidal stability.

The SPIONs synthesized by both methods were characterized by UV–Vis spectroscopy to determine the iron and nanoparticle concentrations, dynamic light scattering (DLS) to measure the hydrodynamic diameter and particle size distribution, and frequency mixing magnetic detection (FMMD) to determine the magnetic core diameter and magnetic properties.

The findings indicate that the proposed green synthesis approach is capable of producing SPIONs with physicochemical and magnetic properties that are comparable to those obtained by the conventional co-precipitation method using aqueous ammonia. Further details and a comprehensive discussion of the results will be presented during the poster session.

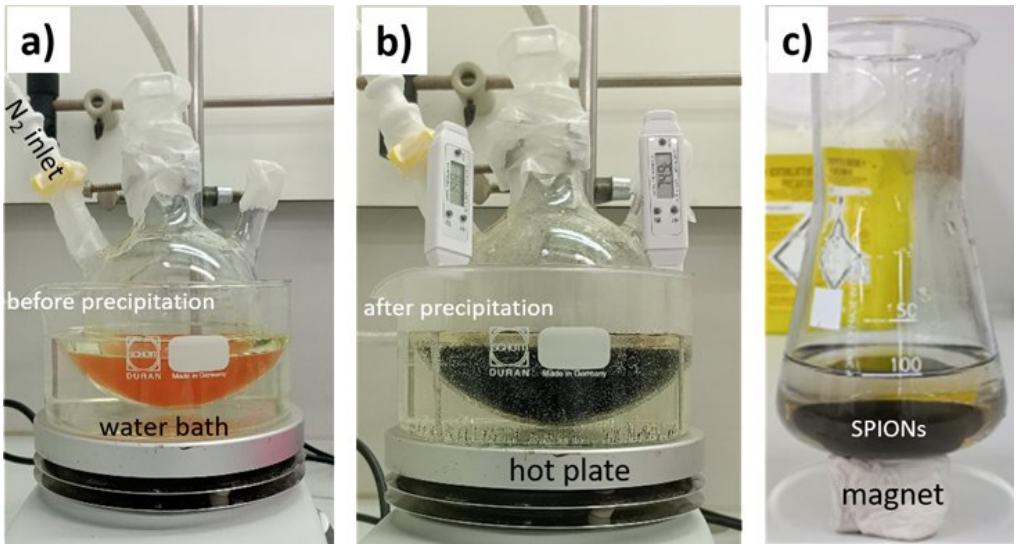

Fig.1: Photographic documentation of the nanoparticle synthesis process, showing (a) the preparation step with mixing of the iron salt precursors, (b) the co-precipitation step after addition of the precipitating agent followed by thermal treatment, and (c) the magnetic separation of the synthesized nanoparticles prior to the washing procedure.

Acknowledgment:

The authors gratefully acknowledge Prof. Hans-Joachim Krause and Prof. Ulrich Engelmann for their valuable support with the FMMD and DLS measurements, respectively, which contributed significantly to this study.

References

[1] R. Qiao, C. Yang, and M. Gao, „Superparamagnetic iron oxide nanoparticles: from preparations to in vivo MRI applications“, *J. Mater. Chem.*, vol. 19, no. 35, pp. 6274, 2009.

[2] J. Estelrich, E. Escribano, J. Queralt, and M. Busquets, „Iron Oxide Nanoparticles for Magnetically-Guided and Magnetically-Responsive Drug Delivery“, *Int. J. Mol. Sci.*, vol. 16, no. 4, pp. 8070–8101, Apr. 2015.

[3] E. C. Abenojar, S. Wickramasinghe, J. Bas-Concepcion, and A. C. S. Samia, „Structural effects on the magnetic hyperthermia properties of iron oxide nanoparticles“, *Prog. Nat. Sci. Mater. Int.*, vol. 26, no. 5, pp. 440–448, Okt. 2016.

[4] W. Wu, Z. Wu, T. Yu, C. Jiang, and W.-S. Kim, „Recent progress on magnetic iron oxide nanoparticles: synthesis, surface functional strategies and biomedical applications“, *Sci. Technol. Adv. Mater.*, vol 16, no. 2, pp. 023501, Apr. 2015.

[5] S. K. Begum *u. a.*, „Green synthesis of magnetite (Fe_3O_4) and hematite (Fe_2O_3) nanoparticles using Moringa oleifera and Psidium guajava leaf extracts for sustainable applications“, *Sci. Rep.*, vol. 15, no. 1, pp. 36465, Okt. 2025.

How materials properties govern signal generation in magnetic particle spectroscopy: First answers from simulative insights

S. Bolte(1), O. Lawal(1), and U. M. Engelmann (1)

(1) Department of Medical Engineering and Applied Mathematics
FH Aachen University of Applied Sciences,
D-52428 Jülich, Germany

E-Mail: sandra.bolte@alumni.fh-aachen.de | engelmann@fh-aachen.de

Abstract – Magnetic nanoparticles (MNP) are promising for therapy (magnetic fluid hyperthermia, MFH) and diagnostics (magnetic particle spectroscopy, MPS; magnetic particle imaging, MPI). Iron oxides are biocompatible, while cobalt-iron nanoparticles, though arguably less biocompatible, offer superior magnetic properties like high saturation magnetization and anisotropy, making them useful for studying intrinsic magnetic effects on MPS signals. This preliminary study employs dynamic magnetization relaxation to explore the influence of saturation magnetization, anisotropy, and associated core size of iron oxides, cobalt ferrite, and cobalt-iron MNP on MPS signal generation, providing first insights into the potential effects of material properties.

Introduction – Due to their superparamagnetic (SPM) nature, magnetic nanoparticles (MNP) are generally promising materials for biomedical applications such as magnetic fluid hyperthermia (MFH), magnetic particle spectroscopy (MPS), and magnetic particle imaging (MPI) [1]. In this work, the MPS signal generation of maghemite (γ-Fe_2O_3), magnetite (Fe_3O_4), cobalt ferrite ($CoFe_2O_4$), and cobalt-iron (CoFe) nanoparticles is predicted using stochastic Néel-Brownian relaxation simulations to investigate the influence of material properties (saturation magnetization and effective anisotropy constant) as well as associated core sizes on the generated MPS signal.

Methods – Stochastic Néel-Brownian coupled relaxation dynamics simulations [2] were performed to investigate the magnetic behavior of four MNP materials: γ-Fe_2O_3, Fe_3O_4, $CoFe_2O_4$ and CoFe. The magnetic properties were defined by their respective saturation magnetization and anisotropy constant: magnetite (M_s = 476 kA·m^{-1}, K =11 kJ·m^{-3}), maghemite (M_s = 425 kA·m^{-1}, K = 5 kJ·m^{-3}), cobalt ferrite (M_s = 490 kA·m^{-1}, K = 150 kJ·m^{-3}) [3, 4] and cobalt-iron (M_s = 1632 kA·m^{-1}, K = 1500 kJ·m^{-3}). All simulations were performed at a particle concentration of 10^{15} mL^{-1}, rendering particles non-interacting [5], and a temperature of 310 K.
Three log-normal core size distribution widths from monodisperse to polydisperse (σ = 0.05, 0.25, and 0.45) were investigated. Magnetite and maghemite were simulated with mean core diameters of $d_C = (16, 20, 24, 28)\, nm$ and two hydrodynamic diameter conditions defined as $d_H = d_C + 10\, nm$ and $d_H = d_C + 100\, nm$. For cobalt ferrite and cobalt-iron nanoparticles, smaller mean core diameters of $d_C = (8, 10, 12, 14)\, nm$ were considered with corresponding hydrodynamic diameters of $d_H = d_C + 10\, nm$ and $d_H = d_C + 100\, nm$. In all cases, core size was chosen to comply with SPM limits. MNP were excited by a sinusoidal alternating magnetic field with an amplitude of 20 $\mathrm{mT} \cdot \mu_0{}^{-1}$ and a frequency of 25 kHz. The resulting differential magnetization (dM/dH) was evaluated as a measure for the MPS signal to compare the influence of the particle material, core size, hydrodynamic diameter, and core size distribution. For comparison between different materials, all signal intensities were normalized on all datasets to an equivalent iron amount by dividing by the MNP-mass $m_{MNP} = \rho_{MNP} n_p exp\left(\frac{9}{2}\sigma^2\right)\frac{\pi}{6} d_C^3$ and subsequently normalized to a global maximum signal intensity.

Results and Discussion – Contour plots in Fig. 1 show the differences in the MPS signal of the investigated nanoparticle materials. Under the investigated simulation conditions, magnetite and maghemite exhibit considerably higher MPS signal intensities than cobalt ferrite and cobalt-iron. In both iron oxide materials, the signal peaks for monodisperse mid-sized particles $d_C \sim (20 - 24)$ nm.
In contrast, cobalt ferrite and cobalt-iron nanoparticles exhibit substantially lower signal intensities,

generally highest for smallest core sizes of d_C~8 nm. The hydrodynamic size affects the signal only marginally by less than 10% independent of core material.

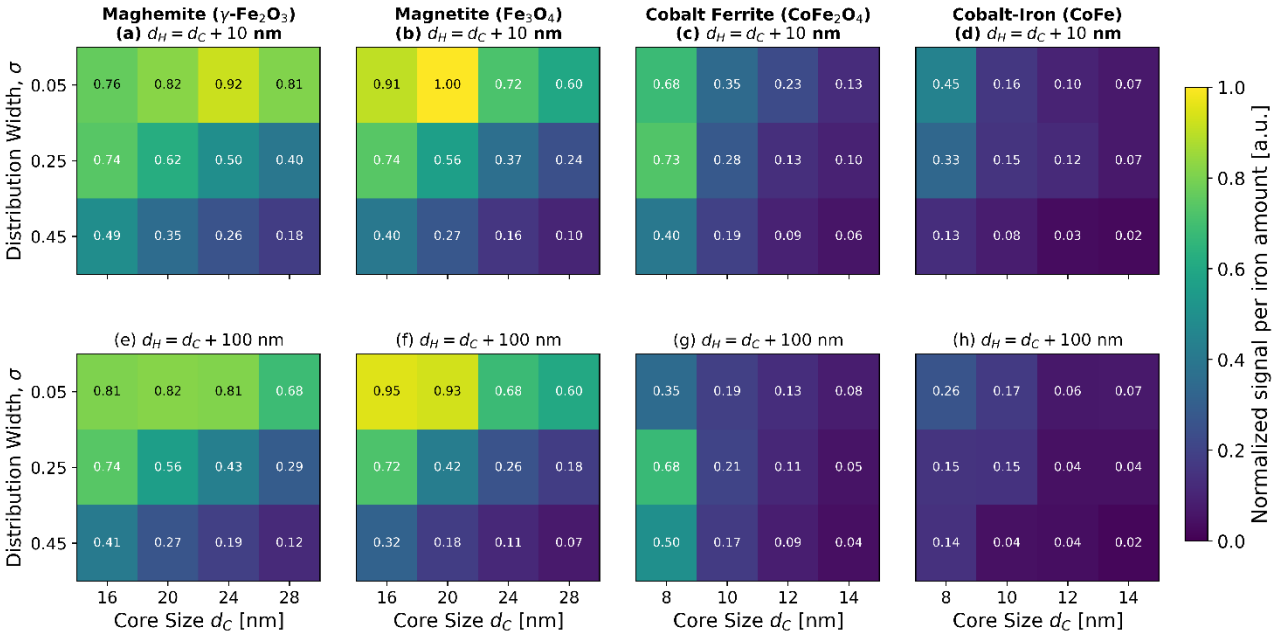

Figure 1: Contour plots showing the normalized dM/dH signal intensity of (a, e) maghemite (γ-Fe_2O_3), (b, f) magnetite (Fe_3O_4), (c, g) cobalt ferrite ($CoFe_2O_4$), and (d, h) cobalt–iron (CoFe) nanoparticles as a function of core size, distribution width, and hydrodynamic diameter. Signal intensities were first converted to an equivalent iron amount and subsequently normalized to the global maximum signal intensity across all materials, enabling direct comparison of the relative signal strengths.

The lower signal intensities for cobalt-associated MNP can be explained by the smaller core diameters used for these particles compared to iron oxide MNP. The magnetic response appears to be more sensitive to the interplay between magnetic material properties and particle size. This behavior is likely related to the considerably higher saturation magnetization and magnetic anisotropy of cobalt-iron.

Conclusion – The presented simulations demonstrate that material-dependent magnetic properties significantly affect the MPS signal. While magnetite and maghemite exhibit comparable trends of maximizing MPS signal for mid-sized core sizes (d_C~$(20-24)$ nm), cobalt-associated MNP exhibit peak MPS signal for smaller particles (d_C~8 nm), suggesting a more complex relationship between particle size and magnetic properties. Future work should extend the investigated parameter space by considering additional core sizes, viscosities, and particle interactions to investigate in-vivo conditions. Such investigations could provide a more comprehensive understanding of material-dependent MPS behavior and support the optimization of nanoparticles for specific MPS applications.

References

[1] H.-J. Krause and U. M. Engelmann, "Fundamentals and Applications of Dual-Frequency Magnetic Particle Spectroscopy: Review for Biomedicine and Materials Characterization," *Advanced Science*, vol. 12, no. 13, Art. no. 2416838, 2025, doi: 10.1002/advs.202416838

[2] U. M. Engelmann, C. Shasha and I. Slabu, “Magnetic Nanoparticle Relaxation in Biomedical Application”, in *Magnetic Nanoparticles in Human Health and Medicine*, 1st ed., C. Caizer, Ed. Hoboken, John Wiley & Sons, 2021, pp. 327–354, doi: 10.1002/9781119754725.ch15.

[3] A. A. de Almeida, F. Fabris, G. S. da Silva, K. R. Pirota, M. Knobel, and D. Muraca, "Control of Anisotropy and Magnetic Hyperthermia Effect by Addition of Cobalt on Magnetite Nanoparticles," *ACS Applied Materials & Interfaces*, vol. 17, no. 9, pp. 13083–13093, 2025, doi: 10.1021/acsami.4c03343

[4] D. Mada et al., "Magnetic Properties of Cobalt Ferrite Synthesized by Mechanical Alloying," *AIP Conference Proceedings*, vol. 1964, no. 1, Art. no. 020003, 2018, doi: 10.1063/1.5038285

[5] U. M. Engelmann et al. „Comparative Modeling of Frequency Mixing Measurements of Magnetic Nanoparticles Using Micromagnetic Simulations and Langevin Theory“, *Nanomaterials*, vol. 11, Art. no. 1257, 2021, doi: 10.3390/nano11051257

Maternal Gait as a Reference Model for Vestibular Stimulation of Preterm Infants: IMU-Based Derivation of a Biomimetic Motion Profile for an Actively Swinging Hammock

Sude Yildirir[(1)], Christine Bremer[(1)], and Andreas Hennig[(1)]

[(1)] Hochschule Ruhr West
University of Appied Sicences

Institute of Measuring and Sensor Technology,
D-45476 Mülheim an der Ruhr

E-Mail: christine.bremer@hs-ruhrwest.de
Web: www.hochschule-ruhr-west.de

Background: Preterm infants lose the continuous, rhythmic movement stimuli of the womb at birth, although these stimuli are essential for vestibular and sensorimotor maturation, and standardized motion parameters for actively swinging hammock systems in neonatal intensive care are still lacking [1], [2].
Against this background, the thesis investigates whether physiologically plausible reference values for vestibular stimulation can be derived from the gait pattern of pregnant women and translated into a technically controllable motion profile for a preterm infant hammock [3], [4], [5].

Methods: For the acquisition of the IMU data, measurements were recorded from two pregnant women in their third trimester during natural walks using a sensor attached to the lower back, and the data were scaled into physical units. In the analysis, the data were filtered with a 5 Hz Butterworth low-pass filter and evaluated in two stable analysis windows [4], [6].From the accelerometer and gyroscope signals, rhythmic, translational, rotational, and safety-related parameters were derived and transferred to a child-related orientation using a simplified 45° projection to approximately account for the uncertain fetal position in the technical derivation [3], [7].

Results: The evaluated dominant step frequency was about 1.68 Hz, which resulted in a gait-cycle frequency of approximately 0.85 Hz. Values lie within the frequency ranges described in the literature for vestibular stimulation in preterm infants. [1]. For translational motion, mean displacement amplitudes of 36.4 mm (Surge), 28.4 mm (Heave), and 26.5 mm (Sway) were derived. This resulted in 45°-projected orientation values of 25.7 mm, 20.1 mm, and 18.7 mm, which can be classified as plausible magnitudes for gentle rocking movements [8], [9] . Rotationally, Roll, Pitch, and Yaw components were identified, whereby Roll at 6.17° appears suitable as a limited secondary component for the hammock, while Pitch and especially Yaw were not adopted as primary target motions for safety reasons [10]. In addition, four application-oriented profiles were derived: a vestibular stimulation profile as the core profile, a sleep and regulation profile, a rest profile, and a passive positioning profile; furthermore, a biomimetic control signal was formulated with a fundamental frequency, harmonic components, and slow amplitude modulation. [1], [8], [9].

Conclusion: The thesis shows that maternal gait can serve as a physiological reference model for motion design in an actively swinging hammock for preterm infants because it provides rhythm, translational displacement, and limited rotation within a range compatible with described vestibular stimulation [1], [2], [11]. At the same time, this work should be understood as an exploratory foundational study, since clinical effectiveness, optimal limits, and the transferability of rotational components still need to be verified in larger validation studies [2], [10].

References

[1] J. Provasi, L. Blanc, and I. Carchon, "The Importance of Rhythmic Stimulation for Preterm Infants in the NICU," *Children (Basel, Switzerland)*, vol. 8, no. 8, 2021, doi: 10.3390/children8080660.

[2] M. G. Prescott, K. Wróblewska-Seniuk, M. Lenells, M. Fiander, R. Soll, and M. Bruschettini, "Vestibular stimulation for promoting development and preventing morbidity in preterm infants," *The Cochrane database of systematic reviews*, vol. 9, no. 9, CD016072, 2024, doi: 10.1002/14651858.CD016072.

[3] S. W. Verbruggen *et al.,* "Modeling the biomechanics of fetal movements," *Biomechanics and modeling in mechanobiology*, vol. 15, no. 4, pp. 995–1004, 2016, doi: 10.1007/s10237-015-0738-1.

[4] M. Boutaayamou *et al.,* "Toward Convenient and Accurate IMU-Based Gait Analysis," *Sensors (Basel, Switzerland)*, vol. 25, no. 4, 2025, doi: 10.3390/s25041267.

[5] M. Branco, R. Santos-Rocha, L. Aguiar, F. Vieira, and A. Veloso, "Kinematic analysis of gait in the second and third trimesters of pregnancy," *Journal of pregnancy*, vol. 2013, p. 718095, 2013, doi: 10.1155/2013/718095.

[6] F. Crenna, G. B. Rossi, and M. Berardengo, "Filtering Biomechanical Signals in Movement Analysis," *Sensors (Basel, Switzerland)*, vol. 21, no. 13, 2021, doi: 10.3390/s21134580.

[7] J. Okemo, E. Gulavi, M. Mwaniki, and S. Wanyonyi, "Abnormal Lie-Presentation," *GLOWM*, 2021, doi: 10.3843/GLOWM.414593.

[8] M. P. Sammon and R. A. Darnall, "Entrainment of respiration to rocking in premature infants: coherence analysis," *Journal of applied physiology (Bethesda, Md. : 1985)*, vol. 77, no. 3, pp. 1548–1554, 1994, doi: 10.1152/jappl.1994.77.3.1548.

[9] C. G. Ribas, M. G. Andreazza, V. C. Neves, and S. Valderramas, "Effectiveness of Hammock Positioning in Reducing Pain and Improving Sleep-Wakefulness State in Preterm Infants," *Respiratory care*, vol. 64, no. 4, pp. 384–389, 2019, doi: 10.4187/respcare.06265.

[10] W.-C. Su, C.-K. Lin, and S.-C. Chang, "A study of safety and tolerability of rotatory vestibular input for preschool children," *Neuropsychiatric disease and treatment*, vol. 11, pp. 41–49, 2015, doi: 10.2147/NDT.S76747.

[11] T. Gujarathi and K. Bhole, "GAIT ANALYSIS USING IMU SENSOR," in *2019 10th International Conference on Computing, Communication and Networking Technologies (ICCCNT)*, Kanpur, India, 2019, pp. 1–5, doi: 10.1109/ICCCNT45670.2019.8944545.

Fluorescence Spectroscopy for Biosignature Detection in Icy Ocean Worlds: Insights from the TRIPLE AstroBioLab

Jacqueline Blok(1), Ilya Digel(1)

(1) Institute for Bioengineering,
FB 9, FH Aachen University of Applied Sciences,
52428, Jülich, Germany
E-Mail: jacqueline.blok@alumni.fh-aachen.de, digel@fh-aachen.de
Web: www.fh-aachen.de

Abstract – Icy ocean worlds of the solar system, such as Europa and Enceladus, are considered prime targets in the search for extraterrestrial life. [1] This search is inherently challenging, as even the definition of life itself remains debated, and single analytical methods may not be sufficient to provide unambiguous information. Integrating multiple complementary analytical methods is essential to gain a comprehensive understanding of potential biosignatures. Our research group is developing an in situ bioanalytical laboratory, the TRIPLE AstroBioLab (ABL), which is intended for field deployment and testing in Antarctica, a terrestrial analog environment for icy ocean worlds. To enhance the reliability of biosignature detection, the ABL integrates a combination of imaging techniques, fluorescence spectroscopy, compact mass spectrometry, and potentially metagenomic analysis. [2]

Within this multimodal framework, fluorescence spectroscopy is a valuable approach for identifying and differentiating biological and organic matter based on the unique optical signatures of biomolecules such as NADH, FAD, chlorophyll, and tryptophan. In icy ocean environments, chromophoric organic compounds and biosignatures may be highly diluted and present only in very low abundances. [3], [4]

Therefore, investigating the capabilities and limitations of the ABL fluorescence spectroscopy module, as well as establishing a reliable basis for spectral identification, are central aspects of this experimental study.

The ABL spectroscopy module operates at four excitation wavelengths (265 nm, 275 nm, 430 nm, 545 nm). The fluorescence emission is recorded using an Ibsen Freedom UV-VIS spectrometer covering 190 – 850 nm with an optical resolution of approximately 1.7 nm. The spectrometer incorporates a Hamamatsu S11639 CMOS detector. Its performance is compared with that of a commercial JASCO FP-8500 spectrofluorometer (JASCO Corporation) using identical samples under comparable measurement conditions to assess the performance of the ABL fluorescence spectroscopy module.

The lowest reliably detectable concentrations are investigated using three consecutive measurements per concentration for selected reference compounds, including tryptophan, humic acid, and water-soluble chlorophyllin sodium salt, as well as microbial cells in laboratory-based Antarctic analog samples. Cell concentrations are determined using ImageJ. In addition, excitation-emission matrices (EEMs) of natural samples from saline aquatic environments, as well as laboratory mock cultures are acquired using the JASCO FP-8500. These measurements are used to establish a spectral reference database for the identification of unknown samples under conditions relevant to icy ocean worlds.

Preliminary results demonstrate that the ABL fluorescence spectroscopy module can detect tryptophan, humic acid, chlorophyllin sodium salt and microbial cells, with preliminary detection limits of 0.4 mg/L (1.96 µM) for tryptophan, 0.2 mg/L (0.29 µM) for chlorophyllin sodium salt, and 0.4 mg/L for humic acid. Compared with the JASCO FP-8500, the ABL module showed a lower signal-to-noise ratio and differences in the observed emission peak positions. For microbial cells excited at 430 nm, a preliminary detection limit of approximately 18 cells/µL was achieved. Further measurements, statistical evaluation and optimization of the ABL fluorescence spectroscopy module are still ongoing.

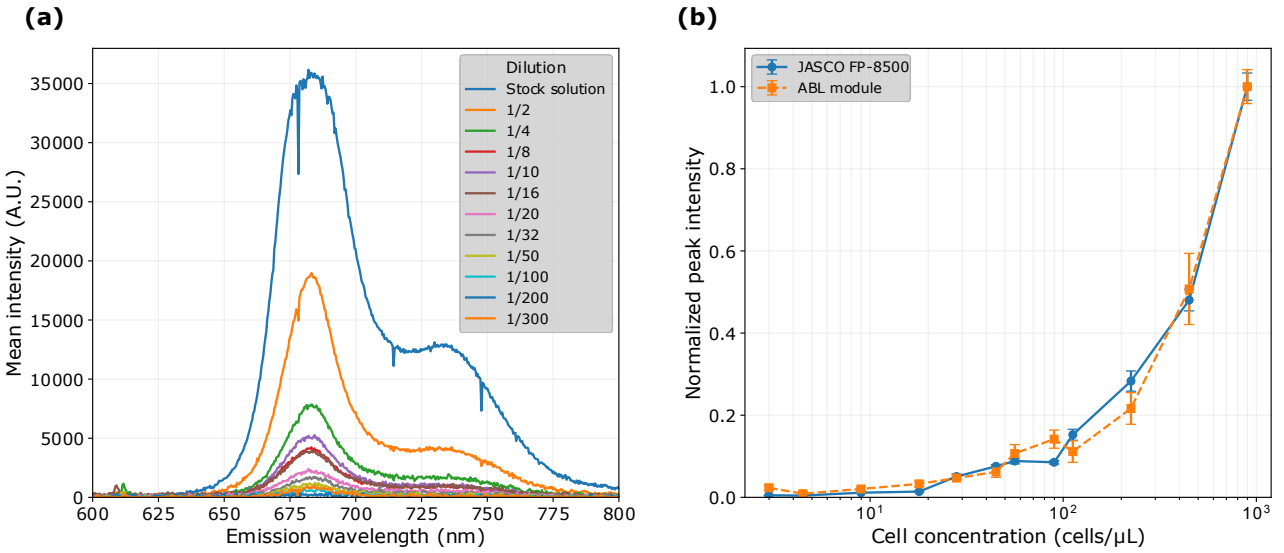

Fig.1: (a) Mean fluorescence emission spectra of microbial cells at different concentrations measured using the ABL fluorescence spectroscopy module at an excitation of 430 nm. (b) Normalized mean fluorescence intensity as a function of cell concentration, determined from three consecutive measurements at the emission of 680 nm. Error bars represent the standard deviation of the three measurements.

References

[1] A. R. Hendrix *et al.*, "The NASA Roadmap to Ocean Worlds," *Astrobiology*, vol. 19, no. 1, pp. 1–27, Jan. 2019, doi: 10.1089/ast.2018.1955.

[2] A. Tepecik *et al.*, "Concept and development of a multimodal bioanalytic laboratory for the in-situ exploration of icy ocean worlds," *Front. Astron. Space Sci.*, vol. 13, Aug. 2026, doi: 10.3389/fspas.2026.1894853.

[3] Z.-P. Zhong *et al.*, "Clean Low-Biomass Procedures and Their Application to Ancient Ice Core Microorganisms," *Front. Microbiol.*, vol. 9, May 2018, doi: 10.3389/fmicb.2018.01094.

[4] E. J. D'Sa, H.-C. Kim, S.-Y. Ha, and I. Joshi, "Ross Sea Dissolved Organic Matter Optical Properties During an Austral Summer: Biophysical Influences," *Front. Mar. Sci.*, vol. 8, Oct. 2021, doi: 10.3389/fmars.2021.749096.

Operating Procedure Adaptation for DNA Sequencing of Sea Water Microbiome for Antarctic Metagenome Analysis

Isabelle Kamp(1)

(1) Institute for Bioenginneering,
Faculty of Medical Engineering and Technomathematics,
Aachen University of Applied Sciences,
D-52428 Jülich, Germany

E-Mail: isabelle.kamp@alumni.fh-aachen.de

Abstract – In the search of signs for extraterrestrial life (biosignatures) on e.g. icy moons like Europa and Enceladus, harsh environments like Antarctica are used as analogues to explore strategies for this search. One of these projects testing strategies for finding biosignatures is the AstroBioLab (ABL) as part of the project TRIPLE (Technologies for Rapid Ice Penetration and subglacial Lake Exploration). The ABL is an integrated system designed for automated non-destructive in-field analysis of water samples, to detect biosignatures by means of microscopy and spectroscopy.
Samples will be gathered by filtering 200-500 mL sea water through a Sterivex™ filter, which is backflushed to yield approximately 12.5 mL of sample that is automatically analyzed in the ABL. The output of the ABL is then shared between a Mass spectrometer and the DNA Sequencing workflow, limiting the sample volume available for sequencing.

While it is uncertain that DNA is an essential molecule of life on other planets and current sequencing technologies are not suitable for use on other planets, search for Life in Antarctic Ocean can be expected to yield positive results of DNA-based life. Sequencing the DNA of gathered samples increases the data yield of the expedition, potentially enables cross-validation of species identification with microscopy and improve scientific knowledge of microbial diversity in terms of species and metabolism.

A small laboratory space in Neumeyer III Station in Antarctica is designated for the DNA Sequencing workflow. This sheltered space will be equipped with a Vortex lab dancer, a BentoLab providing a mini-centrifuge and a thermocycler, an Eppendorf Biophotometer for evaluation, pipets and required consumables.
The sample preparation for DNA sequencing starts with DNA Extraction to increase DNA yield and purity compared to using extracellular DNA. For this step, the Qiagen DNeasy PowerWater kit protocol was adapted to portable laboratory equipment. The kit uses bead beating with buffers for cell lysis and magnetic beads and a binding column for isolation and clean-up of DNA.
The Oxford Nanopore Technologies Rapid Barcoding Kit's protocol, which is used for library preparation, was also adapted. This kit uses a shotgun-approach for tagging DNA and enables multiplexing of samples, so that a sample can be sequenced together with a negative control and possibly also a standardized positive control.
The result is a Standard Operating Procedure specific to the ABL use case with limited sample volume and low biomass, validated with cultured microorganisms and environmental samples from the North Sea.

Interdigitated Electrodes for Biomedical Applications: Theoretical and Experimental Investigation of Geometric Factors

Adrian Klautsch[(1)], Xuan-Thang Vu[(2)], and Maryam Weil[(1)]

[(1)] Faculty of Medical Engineering and Technomathematics
FH Aachen University of Applied Sciences, Campus Jülich,
D-52428 Jülich, Germany

[(2)] Institute of Materials in Electrical Engineering 1,
Faculty of Electrical Engineering and Information Technology,
RWTH Aachen University,
D-52074 Aachen, Germany

E-Mail: adrian.klautsch@alumni.fh-aachen.de; weil@fh-aachen.de
Web: www.fh-aachen.de

Abstract – Reliable measurement of ionic conductivity in liquid media is essential for environmental analytics, process monitoring, and biosensing applications. It is evident that fluctuations in ionic concentration caused by biological and chemical reactions or modification in sample composition directly affect the electrical conductivity of a solution. Additionally, the variation of ion concentration in solution that comes into contact with biomolecules has the capacity to influence their function. Consequently, conductivity sensors have emerged as a valuable tool for the monitoring of biochemical processes. Miniaturized sensors are of particular importance for bioanalytical applications, where only small sample volumes are often available. These sensors are also a key requirement for the development of lab-on-a-chip and point-of-care devices. Interdigitated electrodes (IDEs) offer enhanced sensitivity for miniaturized conductometric measurements while facilitating cost-effective fabrication through their planar design.

In order to maximize the sensitivity of IDEs and ensure that measured resistance values remain within an acceptable range, a sensor's cell constant must be matched to the analytes' expected conductivity range. Cell constants can be determined experimentally, however, an a priori calculation based on the sensor's geometric parameters could enable an application-specific sensor design without the necessity of producing physical prototypes.

In this study, twelve distinct IDE geometries on a sensor card purchased from Sciospec consisting of copper electrodes on FR-4 glass epoxy were experimentally characterized utilizing the technique of electrochemical impedance spectroscopy (EIS). The sensors were exposed to different KCl and NaCl solutions with a wide conductivity range (100 $\mu S \cdot cm^{-1}$ to 100 $mS \cdot cm^{-1}$) and the resulting impedance spectra measured between 10 Hz and 1 MHz.

For each IDE geometry, the optimal frequency range for reliable conductivity measurements was identified from the recorded impedance spectra. The measured conductances were then correlated with the known solution conductivities in order to determine the cell constant, sensitivity and linear measurement range for each sensor design. The cell constants obtained through experimental measurement were then compared with theoretical values derived from the electrode geometry. This was done to evaluate the accuracy of established design models [1]. The plotting and analysis were conducted using the Python programming language.

The experimentally determined cell constants (κ) range from approximately 0.3 to 1.9 cm^{-1}. Increasing the number of fingers (N) while simultaneously decreasing electrode width (w) and interelectrode spacing (d) to maintain a constant active electrode area (A) leads to a reduction in the

cell constant. A similar decrease can be observed if N is increased without decreasing w and d, indicating that N is the most relevant parameter for adjusting the cell constant. Furthermore, the sensitivity of κ to changes in N decreases at higher finger counts, indicating a plateauing trend. These observations align well with literature [2].

The discrepancy between the theoretically and experimentally determined cell constants ranges from less than 1% to almost 30%. In the majority of cases, the theoretical cell constant is found to be less than the experimental value. However, it is evident that these discrepancies are considerably larger for IDEs with constant w and d values compared to those with variable w and d values (see Fig. 1), warranting future investigation. While the analytical expression cannot predict a sensor's cell constant with absolute precision, it is sufficiently accurate for the purpose of an a priori approximation, which can inform decisions regarding the design of sensors.

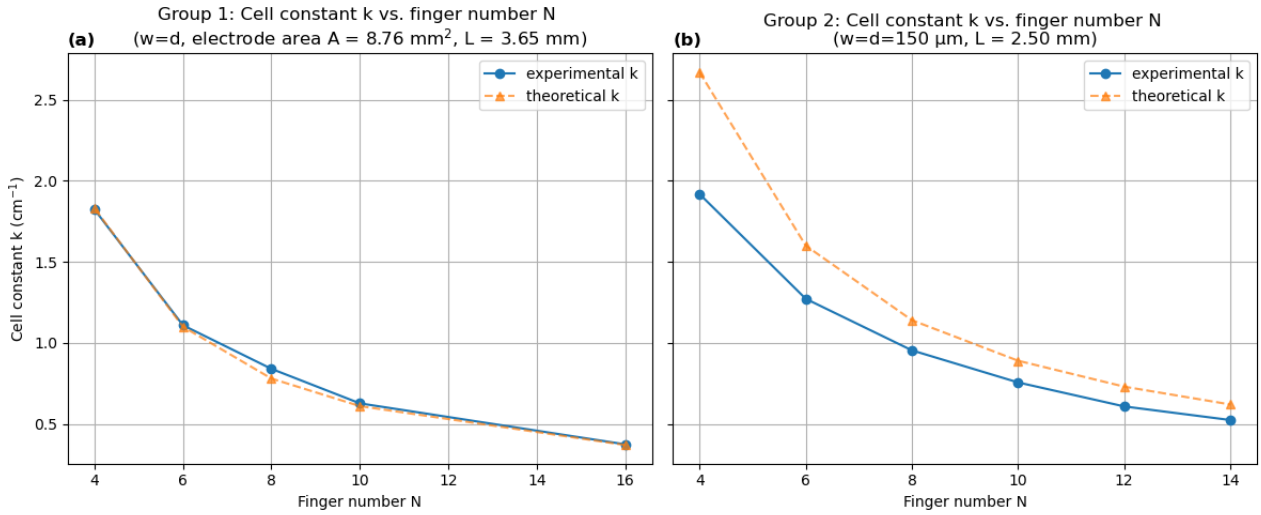

Fig. 1: Theoretically and experimentally determined cell constants κ versus. IDE finger number N. (a) Electrode width w and interelectrode spacing d decrease with increasing N to keep the electrode area A constant. (b) w and d remain constant, resulting in an increase in A with increasing N.

References

[1] W. Olthuis, W. Streekstra and P. Bergveld, "Theoretical and experimental determination of cell constants of planar-interdigitated electrolyte conductivity sensors", *Sensors and Actuators. B, Chemical*, vol. 24 no. 1–3, pp. 252–256, 1995.

[2] M. Ibrahim, J. Claudel, D. Kourtiche and M. Nadi, "Geometric parameter optimization of planar interdigitated electrodes for bioimpedance spectroscopy", *Journal of Electrical Bioimpedance*, vol. 4, pp. 13-22, March 2013.

Developing Structured Knowledge in Higher Education Using Kaizen-Based Learning

Yrza Myktybekova [(1)], Kalampir Zhumagulova [(1)] and Ilya Digel [(2)]

[(1)] Department of Biology, Abai Kazakh National Pedagogical University
Almaty, Republic of Kazakhstan

[(2)] Institute for Bioengineering, FH Aachen – University of Applied Sciences
Jülich, Germany

Email: digel@fh-aachen.de

Abstract – The study examines continuous improvement strategies as a means of enhancing the quality of higher education. We outline the theoretical foundations of Kaizen and examine its potential for supporting structured knowledge formation. Particular emphasis is placed on fostering systems thinking, analytical skills, and sustained learning motivation. An educational intervention study was conducted to evaluate the impact of iterative, incremental improvements in learning activities on students' mastery of biochemical concepts. The study involved 60 students in experimental and control groups who were assessed before and after the intervention. The results indicate that the Kaizen-based approach was associated with an improved understanding of complex biochemical processes, greater engagement in reflective learning, and the development of professional competencies. The findings provide preliminary evidence of the potential effectiveness of continuous improvement strategies in education and highlight their practical relevance for modernizing teaching methods and curriculum design in higher education.

Keywords— structured knowledge, Kaizen-based learning, higher education, biochemical education, science and engineering education, systems thinking, continuous improvement.

The purpose of this study was to theoretically substantiate and experimentally evaluate the effectiveness of Kaizen-based learning for developing structured knowledge. To achieve this goal, we first defined the theoretical foundations of structured biochemical knowledge formation in higher education. Second, we analyzed the instructional potential of Kaizen-based learning and developed a model of knowledge formation. Finally, we conducted an educational intervention study and evaluated its results in terms of knowledge development, analytical thinking, and professional competencies. Based on the findings, we formulated practical recommendations for integrating Kaizen principles into the teaching of complex biomedical and engineering-related disciplines.

Current trends require higher education institutions to prepare competent, adaptable, and professionally qualified graduates. In the context of the rapid development of biomedical sciences and medical technologies, students need not only fundamental knowledge but also a *systematic understanding* of complex biological and biochemical processes relevant to physiological functions, diagnostic methods, and biomedical applications. This is especially important in medical engineering programs, where fragmented knowledge may limit students' ability to connect theoretical concepts with practical and technological tasks. Therefore, the search for innovative educational technologies that enhance cognitive activity, sustained motivation, and structured knowledge formation is of particular importance.

In this context, Kaizen-based learning, grounded in the principles of continuous improvement, gradual development, and active student involvement, is of considerable scientific and practical interest. Its use makes it possible to organize learning as a sequence of small but continuous improvements aimed at deepening knowledge, strengthening analytical thinking, and developing professional competencies. Despite extensive research on educational technologies, the integration of Kaizen principles into the formation of structured knowledge in complex scientific disciplines remains insufficiently explored. Issues related to teaching complex scientific disciplines are widely

discussed in contemporary literature. Much attention is given to systematic knowledge formation, international educational practices, and innovative teaching technologies. According to John Biggs, teaching quality is closely related to the constructive alignment of learning objectives, content, and teaching methods [1]. John Hattie emphasizes the strong impact of active student participation and continuous feedback on learning outcomes [2]. Similarly, Michael Prince and Scott Freeman demonstrate that active learning in the natural sciences improves critical thinking and academic performance [3, 4].

The Kaizen concept, internationally popularized by Masaaki Imai, represents an approach to increasing efficiency through systematic incremental improvement [5, 6]. In the present study, these principles were adapted to education through tasks aimed at progressively improving knowledge acquisition, learning strategies, and students' ability to structure complex information. Modern research also emphasizes the role of metacognitive skills and reflection. Barry Zimmerman notes that self-regulation and reflective abilities contribute to deeper knowledge acquisition and the development of professional competencies [7]. These qualities are especially relevant in medical engineering and other science-based fields, where students must integrate theoretical knowledge with practical and technological applications.

During the educational intervention study, the level of biochemical knowledge in the experimental and control groups was assessed. In parallel, a student survey was conducted to evaluate attitudes toward the educational process and the use of Kaizen-based learning. Analysis of the test results revealed greater improvement in biochemical knowledge scores in the experimental group than in the control group. The most pronounced changes were observed at the analytical and systemic levels, indicating a deeper understanding of biochemical processes and an improved ability to apply knowledge when solving unfamiliar or practical problems. In the control group, changes were less evident and were mainly limited to the recall-based level, involving the reproduction of previously learned information. The survey results also indicated generally positive student perceptions of Kaizen-based learning. Most students reported increased interest in the subject, greater confidence in their abilities, and improved understanding of complex biochemical topics.

These findings are consistent with contemporary approaches to student-centered, active, and process-oriented learning [8, 9]. The systematic implementation of small, incremental changes enhanced students' cognitive engagement and supported their transition from recall-based knowledge to analytical and systemic understanding. This approach may be particularly relevant for science-based and medical engineering programs, where students must integrate diverse multidisciplinary concepts into a coherent professional framework. Our results support the feasibility of integrating Kaizen principles into the educational process and provide preliminary evidence of their potential to promote structured knowledge and key competencies. Further research should focus on expanding the empirical base, investigating long-term effects, and applying this approach in broader educational contexts.

References

[1] J. Biggs and C. Tang, Teaching for Quality Learning at University: What the Student Does, 4th ed. Maidenhead, UK: *Open University Press*, 2011.

[2] J. Hattie, Visible Learning: A Synthesis of Over 800 Meta-Analyses Relating to Achievement. London, UK: *Routledge*, 2009.

[3] M. Prince, "Does active learning work? A review of the research," *Journal of Engineering Education*, vol. 93, no. 3, pp. 223–231, 2004, doi: 10.1002/j.2168-9830.2004.tb00809.x.

[4] S. Freeman, S. L. Eddy, M. McDonough, M. K. Smith, N. Okoroafor, H. Jordt, and M. P. Wenderoth, "Active learning increases student performance in science, engineering, and mathematics," *Proceedings of the National Academy of Sciences of the United States of America*, vol. 111, no. 23, pp. 8410–8415, 2014, doi: 10.1073/pnas.1319030111.

[5] M. Imai, Kaizen: The Key to Japan's Competitive Success. New York, NY, USA: *McGraw-Hill*, 1986.

[6] J. K. Liker and G. L. Convis, The Toyota Way to Lean Leadership: Achieving and Sustaining Excellence through Leadership Development. New York, NY, USA: *McGraw-Hill*, 2012.

[7] B. J. Zimmerman, "Becoming a self-regulated learner: An overview," T*heory Into Practice*, vol. 41, no. 2, pp. 64–70, 2002, doi: 10.1207/S15430421TIP4102_2.

[8] A. E. Abylkasymova and B. A. Turgunbaeva, Theory and Methods of Teaching. Almaty, Kazakhstan: Bilim, 2019 [in Russian].

[9] Z. T. Sadvakasova, Higher Education Pedagogy. Almaty, Kazakhstan: Qazaq University, 2020 [in Russian].

Organizing Board

FH AACHEN
UNIVERSITY OF APPLIED SCIENCES

UNIVERSITÄT
DUISBURG
ESSEN

HOCHSCHULE
HAMM-LIPPSTADT

HRW
HOCHSCHULE RUHR WEST
UNIVERSITY OF APPLIED SCIENCES

Westfälische
Hochschule

Contact

yra@fh-aachen.de

www.yra.fh-aachen.de

DOI: 10.17185/duepublico/87574
URN: urn:nbn:de:hbz:465-20260914-161535-9